Structure, Dynamics, and Thermodynamics of the Structural Domain of Troponin C in Complex with the Regulatory Peptide 1−40 of Troponin I[†,‡]

Pascal Mercier,[§] Leo Spyracopoulos,[||] and Brian D. Sykes*,[§]

CIHR Group in Protein Structure and Function, Department of Biochemistry, University of Alberta, Edmonton, Alberta, Canada T6G 2H7, and Department of Biochemistry, University of Alberta, Edmonton, Alberta, Canada T6G 2H7

Received April 12, 2001; Revised Manuscript Received June 22, 2001

ABSTRACT: The structure of the calcium-saturated C-domain of skeletal troponin C (CTnC) in complex with a regulatory peptide comprising residues 1−40 (Rp40) of troponin I (TnI) was determined using nuclear magnetic resonance (NMR) spectroscopy. The solution structure determined by NMR is similar to the structure of the C-domain from intact TnC in complex with $TnI_{1−47}$ determined by X-ray crystallography [Vassylyev, D. G., Takeda, S., Wakatsuki, S., Maeda, K., and Maeda, Y. (1998) *Proc. Natl. Acad. Sci. U.S.A. 95*, 4847−4852]. Changes in the dynamic properties of $CTnC \cdot 2Ca^{2+}$ induced by Rp40 binding were investigated using backbone amide ^{15}N NMR relaxation measurements. Analysis of NMR relaxation data allows for extraction of motional order parameters on a per residue basis, from which the contribution of changes in picosecond to nanosecond time scale motions to the conformational entropy associated with complex formation can be estimated. The results indicate that binding of Rp40 decreases backbone flexibility in CTnC, particularly at the end of the C-terminal helix. The backbone conformational entropy change $(-T\Delta S)$ associated with binding of Rp40 to $CTnC \cdot 2Ca^{2+}$ determined from ^{15}N relaxation data is 9.6 ± 0.7 kcal mol^{-1} at 30 °C. However, estimation of thermodynamic quantities using a structural approach [Lavigne, P., Bagu, J. R., Boyko, R., Willard, L., Holmes, C. F., and Sykes, B. D. (2000) *Protein Sci. 9*, 252−264] reveals that the change in solvation entropy upon complex formation is dominant and overcomes the thermodynamic "cost" associated with "stiffening" of the protein backbone upon Rp40 binding. Additionally, backbone amide ^{15}N relaxation data measured at different concentrations of $CTnC \cdot 2Ca^{2+} \cdot Rp40$ reveal that the complex dimerizes in solution. Fitting of the apparent global rotational correlation time as a function of concentration to a monomer−dimer equilibrium yields a dimerization constant of $\sim$8.3 mM.

Sliding of the thin filament past the thick filament constitutes the mechanical basis of muscle contraction. The thick filament is comprised of three major components (actin, tropomyosin, and the troponin complex), whereas the thick filament consists mainly of myosin. Regulation of muscle contraction occurs at the level of troponin, where binding of Ca^{2+} triggers a cascade of altered protein−protein interactions, leading to force development. Troponin is a three-component complex involving troponin C (TnC),[1] TnI, and TnT. TnC responds to the Ca^{2+} signal; TnI is thought to inhibit interactions between thick and thin filaments in the absence of Ca^{2+}, and TnT is believed to anchor troponin to actin and transmit the Ca^{2+} signal along the thin filament, thereby enhancing the actomyosin ATPase activity from which energy is derived (for reviews, see refs *1−6*).

X-ray and NMR structural studies of TnC reveal a dumbbell-shaped molecule with two globular domains (designated N and C, for the N- and C-terminal domains, respectively) connected by a central linker (*7−11*). Each domain contains two helix−loop−helix EF hand motifs typical of calcium binding proteins (*12*). Sites III and IV in the C-domain are believed to be fully occupied by either Ca^{2+} or Mg^{2+} under physiological conditions, whereas sites I and II in the N-domain are Ca^{2+} specific sites with weaker affinity (see the reviews listed above and ref *13*). Following Ca^{2+} binding to TnC in either of the globular domains, a hydrophobic "pocket" becomes exposed, which constitutes an important binding site for different portions of TnI (for a review, see ref *14* and references therein).

The interaction between the Ca^{2+}-binding and inhibitory proteins of the troponin complex is central to the regulation of muscle contraction. While much is known about how Ca^{2+} induces structural changes in the regulatory domain of TnC and initiates a cascade of protein−protein interactions leading

* To whom correspondence should be addressed. E-mail: brian.sykes@ualberta.ca. Phone: (780) 492-5460. Fax: (780) 492-0886.

§ CIHR Group in Protein Structure and Function, Department of Biochemistry.

|| Department of Biochemistry.

[1] Abbreviations: TnC, troponin C; NTnC, N-domain (residues 1−90) of recombinant chicken skeletal TnC; CTnC, C-domain (residues 88−162) of recombinant chicken skeletal TnC; TnI, troponin I; TnT, troponin T; Rp40, N-terminal synthetic peptide (residues 1−40) of rabbit TnI; $TnI_{96−115}$, inhibitory synthetic peptide (residues 96−115) of chicken skeletal TnI; NMR, nuclear magnetic resonance; HSQC, heteronuclear single-quantum coherence; NOE, nuclear Overhauser effect; τ_m, global rotational correlation time; τ_e, internal correlation time for fast internal motion; S^2, order parameter; DTT, *threo*-1,4-dimercapto-2,3-butanediol; DSS, 2,2-dimethyl-2-silapentane-5-sulfonic acid.

to muscle contraction, much less is known about TnC interactions with TnI and TnT. Neutron scattering studies have shed some light on the general aspects of the TnI–TnC interaction (*15, 16*) in the binary complex and in the presence of TnT (*17*), but despite several years of investigation, there are still no high-resolution structures of the complex, due in part to the low solubility of TnI. A common approach to investigating the sites of interactions between TnC and TnI involves the use of relatively short synthetic fragments of TnI complexed with TnC (*18–34*).

The first 40 residues of TnI (Rp40) represent a region of particular interest. This segment of TnI was first shown by Syska et al. (*35*) to bind to TnC, and further work by Ngai et al. (*36*) established that Rp40 could effectively compete with the inhibitory peptide $TnI_{104-115}$ and block its inhibitory properties with respect to contraction. Later, Tripet et al. (*21*) showed that the ability of Rp40 to compete with $TnI_{104-115}$ is modulated by other TnC-TnI interactions, mainly by the interaction of $TnI_{116-131}$ with the N-domain of TnC (NTnC). These results were corroborated in our previous study with Rp40 (*22*), where we demonstrated, using solution NMR spectroscopic techniques, that Rp40 and TnI_{96-115} share common binding sites on CTnC, but that the interaction of Rp40 is much stronger (Rp40, $K_d = 2 \pm 1$ μM; TnI_{96-115}, $K_d = 47 \pm 7$ μM) and that Rp40 could displace TnI_{96-115} in the absence of NTnC and any other portion of TnI. The exact nature of the structural and/or functional role of Rp40 is still not yet fully understood. The crystal structure of TnC in complex with TnI_{1-47} determined by Vassylyev et al. (*34*) revealed that TnI_{3-33} forms a long α-helix that binds within the hydrophobic pocket of CTnC. The corresponding region of cardiac TnI_{33-80} has also been shown to bind within the hydrophobic patch of the C-domain of cardiac TnC (*30, 31*).

NMR spectroscopy not only is of great utility for probing the atomic structures of proteins but also has proven to be a powerful tool for the study of dynamic and thermodynamic properties of proteins through backbone amide ^{15}N and ^{13}C/^{2}H side chain relaxation measurements (*37–40*). The model-independent approach to relaxation data analysis introduced by Lipari and Szabo allows for extraction of a global macromolecular rotational correlation time (τ_m), as well as an internal correlation time (τ_e) and an order parameter (S^2) that is related to the amplitude of internal motion for each residue (*41, 42*). S^2 can be interpreted as the orientational probability distribution of a given bond vector (N–H or C–H); thermodynamic parameters such as entropy and heat capacity can be estimated in a semiquantitative fashion from changes in S^2 obtained upon ligand binding, or temperature changes (*43*). These approaches have been useful in furthering our understanding of the role of time-dependent conformational fluctuations involved in the binding of metal ions and peptides, for example, and can provide insight into understanding the contribution of dynamics to the overall stability of a protein.

In this paper, we have determined the solution structure of the Ca^{2+}-saturated state of CTnC in complex with the Rp40 peptide using NMR spectroscopy, and performed a series of NMR relaxation experiments to investigate changes in backbone dynamics induced by binding of Rp40. The changes in backbone dynamics were used to estimate the contribution of backbone conformational entropy to the thermodynamics of peptide binding. The solution structure

of $CTnC\cdot2Ca^{2+}$ in the $CTnC\cdot2Ca^{2+}\cdot Rp40$ complex was found to be similar to the structure of CTnC in the crystal structure of $TnC\cdot2Ca^{2+}\cdot TnI_{1-47}$ (*34*).

EXPERIMENTAL PROCEDURES

Construction of the Plasmid Vector Encoding CTnC and Protein Isolation. The engineering of CTnC (residues 88–162) into expression vector pET3a was carried out as described for NTnC (residues 1–90) (*44*) except for the use of two different oligonucleotides that are complementary to the sequence and restriction enzyme sites. The expression and purification of [^{15}N]CTnC and [^{13}C,^{15}N]CTnC in minimal media follows the procedure described for [^{15}N]NTnC (*44, 45*). During expression in *Escherichia coli*, the N-terminal methionine, corresponding to the initiation codon, is not cleaved off. Decalcification of both [^{15}N]CTnC and [^{13}C/^{15}N]CTnC was as described for [^{15}N]NTnC (*45*). Since CTnC has a higher affinity for Ca^{2+} than NTnC, the pH of the 25 mM NH$_4$HCO$_3$ buffer was increased to 8.5 for the decalcification step to increase the efficiency of EDTA. Unlabeled Rp40 peptide, acetyl-GDEEKRNRAITARRQHLKSVML-QIAATELEKEEGRREAEK-amide, was synthesized and purified as described by Ngai and Hodges (*36*).

NMR Sample Preparation. [^{15}N]CTnC and [^{13}C,^{15}N]CTnC were dissolved in 600 μL of NMR buffer (treated with Chelex 100 to remove metal contaminants) containing 100 mM KCl, 10 mM imidazole, and 15 mM DTT in a 90% H$_2$O/10% D$_2$O mixture. Since Rp40 has very low solubility in aqueous solution, it was slowly added in solid form directly to the sample, until a precipitate was observed. To facilitate peptide solubilization, the pH of the solution prior to Rp40 addition was increased to 8.5. After complete dissolution of Rp40, the pH of the final sample was adjusted to 6.8 if necessary (uncorrected for ^{2}H isotope effects). The solution was then filtered, and 480 μL was transferred into an NMR tube, to which 10 μL of 1 M DSS and 10 μL of 1.3% NaN$_3$ were added. The protein and peptide concentrations were determined to be 1.33 and 1.91 mM, respectively, by amino acid analysis in duplicate, corresponding to a peptide/protein ratio of 1.44.

NMR Experiments for Structure Determination. The chemical shift assignment of $CTnC\cdot2Ca^{2+}$ not bound to Rp40 was based on the chemical shift assignment of $TnC\cdot4Ca^{2+}$ previously reported by Slupsky et al. (*9*). For $CTnC\cdot Ca^{2+}$ in the $CTnC\cdot Ca^{2+}\cdot Rp40$ complex, the assignment of ^{1}H, ^{13}C, and ^{15}N resonances, and the subsequent structural determination, were carried out using the results of NMR experiments listed in Table 1. The aromatic protons of Phe residues are unassigned. The two-dimensional (2D) ^{15}N- and ^{13}C-filtered DIPSI and NOESY experiments did not allow for the assignment of Rp40 resonances, due to line broadening as a result of chemical exchange, and poor chemical shift dispersion for the peptide resonances. All NMR spectra were acquired at 30 °C on Varian INOVA 500 MHz, Unity 600 MHz, or INOVA 800 MHz spectrometers (see Table 1) equipped with 5 mm triple-resonance probes and *z*-axis pulsed field gradients for the 500 and 600 MHz instruments and triple-axis gradients for the 800 MHz spectrometer. All experimental FIDs were processed using the program NMRpipe (*46*) and analyzed using either PIPP (*46*) or NMRView programs (*47*). Generally, linear prediction for

Table 1: NMR Experiments Conducted for the Purpose of Chemical Shift Assignment and Obtaining NOE-Based Distance Restraints

	nuclei[a]	^{1}H	nt[b]	x-pts[c]	y-pts	z-pts	x-sw	y-sw	z-sw	mix[d]	ref
^{15}N HSQC	^{1}H, ^{15}N	600	16	960	256	−	7500	1800	−	−	*83, 84*
DISPI-HSQC	^{1}H, ^{1}H, ^{15}N	600	12	1024	256	64	8000	6550	1690	−	*85*
HCCH-TOCSY	^{1}H, ^{1}H, ^{13}C	500	16	768	256	64	6000	3200	3000	−	*86*
CBCA(CO)NNH	^{1}H, ^{13}C, ^{15}N	500	32	768	100	64	6000	7794	1650	−	*83*
HNCACB	^{1}H, ^{13}C, ^{15}N	500	32	1024	108	72	600	7794	1500	−	*83*
^{15}N NOESY-HSQC	^{1}H, ^{1}H, ^{15}N	600	12	1024	256	64	8000	6579	1700	125	*85*
^{15}N NOESY-HSQC	^{1}H, ^{1}H, ^{15}N	600	12	1024	256	64	8000	6579	1700	50	*85*
^{13}C/^{15}N NOESY[e]	^{1}H, ^{1}H, ^{13}C/^{15}N	800	16	1088	280	72	10000	9000	4243	75	*87*
HNHA	^{1}H, ^{1}H, ^{15}N	600	8	1024	152	96	8000	4807	1650	−	*50*
HNHB	^{1}H, ^{13}C, ^{13}C(O)	500	16	902	256	72	6200	4900	1500	−	*88*
^{15}N- and ^{13}C-filtered DIPS[f]	^{1}H, ^{1}H	500	128	4096	1024	−	6200	6200	−	−	*89*
^{15}N- and ^{13}C-filtered NOESY[f]	^{1}H, ^{1}H	500	128	4096	1024	−	6200	6200	−	−	*89*

[a] The nucleus acquired in each dimension (e.g., ^{1}H, ^{15}N indicates proton x, nitrogen y). [b] The number of transients acquired for each FID. [c] x-, y-, and z-pts and -sw are the number of complex points and the sweep width in each respective dimension (x is the directly detected dimension). [d] Mixing times are given in milliseconds. [e] ^{13}C/^{15}N NOESY-HSQC is simultaneously ^{13}C- and ^{15}N-edited NOESY-HSQC. [f] The sequence was heavily modified in-house (L. Spyracopoulos).

up to half the number of experimental points was used in indirect dimensions. Data were then zero-filled to twice the number of acquired plus predicted points, and typically multiplied by a sine-bell apodization function shifted by 60−90° before Fourier transformation.

Distance and Torsion Angle Restraints. Proton−proton distance restraints were derived from measured peak intensities in the three-dimensional (3D) ^{15}N NOESY-HSQC and simultaneous 3D ^{15}N/^{13}C NOESY-HSQC experiments and calibrated as previously described (*48*) with the error on the peak intensities set to 40%, and the lower bound on all proton−proton restraints set to 1.7 Å. The ^{1}H resonances of Rp40 could not be assigned; thus, only symmetry-related cross-peaks were selected from the simultaneous 3D ^{15}N/^{13}C NOESY-HSQC spectrum, minimizing the probability of misinterpretation of a protein−peptide NOE as a protein−protein NOE. Approximately 80 ambiguous contacts, thought to be proton−proton NOE contacts between CTnC·2Ca^{2+} and Rp40, were excluded from structure calculations. Intramolecular CTnC·2Ca^{2+} NOEs within the CTnC·2Ca^{2+}·Rp40 complex with distance violations of >0.3 Å were closely examined before further rounds of structure refinement. On the basis of homologous calcium binding sites, 11 Ca^{2+} distance restraints of 2.0−2.8 Å for sites III and IV were incorporated (*49*). Unfortunately, CTnC·2Ca^{2+}·Rp40 NOE distance restraints were not incorporated, due to ambiguity in the assignment of peptide resonances.

Backbone ϕ dihedral angle restraints were obtained from $^3J_{HNH\alpha}$ coupling constants derived from the 3D HNHA spectrum (*50*). For the HNHA experiment, a correction factor of 1.055 was used (*48*). The peak intensities were assumed to have errors equal to the noise level, and the minimum restraint range was set to ±20°. The backbone ψ dihedral angle was determined from the $d_{N\alpha}/d_{\alpha N}$ ratio as previously described. For $d_{N\alpha}/d_{\alpha N}$ ratios of >1.2, ψ was restricted to −30 ± 110°. For $d_{N\alpha}/d_{\alpha N}$ ratios of <0.71, ψ was limited to −120 ± 100°. Methylene hydrogens for 14 residues were stereospecifically assigned by comparing intraresidue $^1H_N-$ $^1H_{\beta1}$ and $^1H_N-^1H_{\beta2}$ cross-peak intensities in a short-mixing time 3D ^{15}N-edited DIPSI-HSQC experiment (50 ms) (*51*), carefully inspecting intraresidue $^1H_N-^1H_{\beta1}$ and $^1H_N-^1H_{\beta2}$ NOE cross-peak intensities from the 3D ^{15}N-edited NOESY-HSQC spectrum (50 ms) and the 3D simultaneous ^{15}N- and ^{13}C-edited NOESY-HSQC spectrum (75 ms), comparing

intraresidue $^1H_\alpha-^1H_{\beta1}$ and $^1H_\alpha-^1H_{\beta2}$ NOE cross-peak intensities from the 3D simultaneous ^{15}N- and ^{13}C-edited NOESY-HSQC spectrum (75 ms), and carefully inspecting intraresidue $^1H_N-^1H_{\beta1}$ and $^1H_N-^1H_{\beta2}$ cross-peak intensities from a 3D ^{15}N-edited HNHB spectrum. Restraints for the χ_1 angle of 60, 180, or −60° (±60°) were imposed if the results from the three experiments were consistent with a single side chain rotamer. In later stages of the structure refinement, direct refinement against $^{13}C_\alpha$ and $^{13}C_\beta$ chemical shifts for residues located in regions of well-defined secondary structure was employed to further restrain both ϕ and ψ backbone dihedral angles (*52*).

Structures were generated with Xplor 3.1 (*53*) using a simulated annealing protocol with 10 000 high-temperature steps and 7000 cooling steps. The type and number of distance and dihedral restraints are summarized in Table 2. Starting from an extended conformation, we generated an initial set of 100 structures using only NOE-derived distance restraints to probe incorrect NOEs. Following removal of any NOEs yielding distance violations of >0.2 Å from the starting set of restraints, the Vadar (D. S. Wishart, L. Willard, and B. D. Sykes, unpublished) and Procheck (*54*) programs were used to identify the well-defined secondary structure elements from the 30 lowest total energy structures taken from the initial 100 structures, and ϕ angle restraints were applied for subsequent rounds of refinement. The structure was further refined by successively including ψ and χ_1 angle restraints and Ca^{2+} distance restraints in sites III and IV and directly refining against $^{13}C_\alpha$ and $^{13}C_\beta$ chemical shifts. The structural statistics presented in Table 2 are for the 30 structures of lowest total energy obtained from a set of 30 low-energy structures taken from an ensemble of 100 structures generated from an elongated conformation, after refinement of the structure was complete.

Backbone Amide ^{15}N Relaxation Measurements. All relaxation data were acquired at 30 °C on Varian INOVA 500 MHz and Unity 600 MHz spectrometers. Sensitivity-enhanced pulse sequences developed by Farrow et al. (*37*) were used to measure $^{15}NT_1$, $^{15}NT_2$, and {^{1}H}−^{15}N NOE values.

Prior to the addition of Rp40, backbone amide ^{15}N backbone relaxation data for [^{15}N]CTnC·2Ca^{2+} were collected at 500 MHz. The same NMR sample ([^{15}N]CTnC· 2Ca^{2+}·Rp40) was used for structure determination and backbone relaxation measurements. Due to partial dimer-

Table 2: Structural Statistics for CTnC·2Ca^{2+} in the CTnC·2Ca^{2+}·Rp40 Complex

no. of NOE restraints	
total	873
intraresidue	447
sequential ($\lvert i - j \rvert = 1$)	208
medium-range ($2 \leq \lvert i - j \rvert \leq 4$)	140
long-range ($\lvert i - j \rvert \geq 5$)	78
no. of dihedral restraints	
total	86
ϕ	33
φ	32
χ_1	21
no. of restraints violations	
distance > 0.1 Å	7 (0.23/str.)
dihedral angle > 1°	1 (0.03/str.)
rmsd to averaged structure (Å)	
well-defined regions^a (N, C$_\alpha$, C)	0.63 ± 0.14
all regions^b (N, C$_\alpha$, C)	0.77 ± 0.17
heavy atoms	0.80 ± 0.17
helix E (residues 95−105)	0.36 ± 0.15
helix F (residues 116−124)	0.25 ± 0.15
helix G (residues 131−141)	0.26 ± 0.09
helix H (residues 151−158)	0.24 ± 0.06
β-sheets (residues 112−114, 148−150)	0.22 ± 0.08
energies^c (kcal mol^{-1})	
E_{total}	348 ± 4
E_{NOE}	1.4 ± 0.5
$E_{dihedral}$	0.03 ± 0.02
$\phi-\psi$ in core or allowed regions^d (%)	
residues in most favored regions	84.6
residues in additional allowed regions	14.9
residues in generously allowed regions	0.3
residues in disallowed regions	0.1

^{a} Using residues 95−158 having backbone rmsds of <1.00. ^{b} Using residues 95−158. ^{c} Using all residues in the first 30 lowest-energy structures. ^{d} Using residues 95−158, as determined by the program Procheck (54).

ization of the CTnC·2Ca^{2+}·Rp40 complex in solution (see Results), backbone amide ^{15}N NMR relaxation data were collected at three different concentrations of the protein−peptide complex at 600 MHz (1.33, 0.65, and 0.33 mM by consecutively diluting the same sample by a factor of 2) and at the initial (1.33 mM) and final protein concentration (0.33 mM) at 500 MHz. The protein and Rp40 concentrations were determined in duplicate by amino acid analysis after each dilution.

All ^{15}NT_1, ^{15}NT_2, and {^{1}H}−^{15}N NOE experiments were collected with 794 (t_1) × 96 (t_2) complex points at 500 MHz and 970 (t_1) × 96 (t_2) complex points at 600 MHz. The T_1 relaxation delays were 11.1, 55.5, 122.1, 199.8, 277.5, 388.5, 499.5, 666, 888, and 1100 ms on both instruments. The delay between repetitions of the pulse sequence was set to 1.2 s for the T_1 experiment. The T_2 relaxation delays were set to 16.61n and 16.544n ms (where n = 1, 2, ..., 10) on the 500 and 600 MHz spectrometers, respectively. For the T_2 experiment, the delay between repetitions of the pulse sequence was 3 s at 500 and 600 MHz. {^{1}H}−^{15}N NOEs were measured in the absence (incorporating a relaxation delay of 5 s between repetitions of the pulse sequence) and presence of proton saturation (incorporating 3 s of ^{1}H saturation, and a delay between repetitions of the pulse sequence of 2 s). All relaxation data were processed using the NMRpipe program (46) and analyzed using PIPP (55) or NMRView (47). The data were processed as described above, with the exception that linear prediction was not used.

Analysis of Backbone Amide ^{15}N Relaxation Measurements. Magnetic dipole−dipole interactions between the ^{15}N nucleus and the amide ^{1}H, and the chemical shift anisotropy of the ^{15}N nucleus, are the predominant relaxation mechanisms contributing to macroscopic relaxation times T_1, and T_2, and cross-relaxation giving rise to the {^{1}H}−^{15}N NOE, for a given backbone amide ^{15}N. The ^{15}NT_1, ^{15}NT_2, and {^{1}H}−^{15}N NOE relaxation parameters are theoretically well established (37, 56) and are expressed as a linear combination of a spectral density function at the resonance frequencies of ^{15}N and ^{1}H$_N$ nuclei:

$$\frac{1}{T_1} = d^2[J(\omega_H - \omega_N) + 3J(\omega_N) + 6J(\omega_H + \omega_N)] + c^2[J(\omega_N)] \quad (1)$$

$$\frac{1}{T_2} = \frac{d^2}{2}[4J(0) + J(\omega_H - \omega_N) + 3J(\omega_N) + 6J(\omega_H + \omega_N) + 6J(\omega_H)] + \frac{c^2}{6}[4J(0) + 3J(\omega_N)] + R_{ex} \quad (2)$$

$$\text{NOE} = 1 + \frac{\gamma_H}{\gamma_N}d^2[6J(\omega_H + \omega_N) - J(\omega_H - \omega_N)]T_1 \quad (3)$$

where $d^2 = (0.1\gamma_H^2\gamma_N^2\hbar^2)/(4\pi^2 r_{NH}^6)$, $c^2 = \frac{2}{15}\gamma_N^2 H_0^2(\sigma_\parallel - \sigma_\perp)^2$, γ_H is the proton magnetogyric ratio (2.68×10^8 rad s^{-1} T^{-1}), γ_N is the magnetogyric ratio of ^{15}N (-2.71×10^7 rad s^{-1} T^{-1}), r_{NH} is the proton−nitrogen internuclear distance (1.02 Å), $\sigma_\parallel$ and $\sigma_\perp$ are the principal components of the ^{15}N chemical shift anisotropy (CSA) tensor [$(\sigma_\parallel - \sigma_\perp)^2 = -160$ ppm], $\hbar$ is Planck's constant divided by 2π (1.05×10^{-34} J s), H_0 is the strength of the magnetic field, ω_N is the Larmor frequency of ^{15}N, ω_H is the Larmor frequency of ^{1}H$_N$, and R_{ex} (s^{-1}) accounts for the contribution of potentially genuine microsecond to millisecond time scale internal motions, in a phenomenological fashion. The second-rank chemical shift anisotropy tensor for the ^{15}N nucleus was assumed to be axially symmetric, and parallel to the amide ^{15}N−^{1}H$_N$ bond vector.

Backbone amide ^{15}N NMR relaxation data were interpreted using the Lipari−Szabo model-free approach (41, 42), where the spectral density function $J(\omega)$ is expressed as

$$J(\omega) = \frac{2}{5}\left[\frac{S^2\tau_m}{1 + \omega^2\tau_m^2} + \frac{(1 - S^2)\tau}{1 + \omega^2\tau^2}\right] \quad (4)$$

where $\tau^{-1} = \tau_m^{-1} + \tau_e^{-1}$, S^2 (the order parameter) accounts for the degree of spatial restriction for a backbone amide ^{15}N−^{1}H$_N$ bond vector and ranges from 0 to 1, with 0 indicating completely unrestricted internal motion and 1 indicating completely restricted internal motion, τ_m is the global molecular rotational correlation time, and τ_e is the correlation time for fast internal motions ($\tau_e \ll \tau_m$). When internal motions occur on two different time scales, eq 4 can be extended in a heuristic fashion:

$$J(\omega) = \frac{2}{5}\left[\frac{S^2\tau_m}{1 + \omega^2\tau_m^2} + \frac{(S_f^2 - S^2)\tau_s'}{1 + \omega^2\tau_s'^2}\right] \quad (5)$$

where $S^2 = S_f^2 S_s^2$, $\tau_s' = \{\tau_s \tau_m\}/\{(\tau_s + \tau_m)\}$, S_f^2 describes the order parameter for fast picosecond internal motions, S_s^2 is the order parameter for nanosecond time scale internal motions faster than τ_m but slower than τ_e, and τ_s is a correlation time for nanosecond time scale internal motions (*57, 58*). The correlation time for picosecond internal motions is assumed not to contribute to relaxation.

Analysis of Backbone Amide ^{15}N Relaxation Measurements. The experimental backbone amide relaxation parameters for each residue were fit using five different models for the spectral density function [$S^2-\tau_m$, $S^2-\tau_m-\tau_e$, $S^2-\tau_m-R_{ex}$, $S^2-\tau_m-\tau_e-R_{ex}$, and a two-time scale model (*57, 58*)]. For each residue, parameters for each model of the spectral density function were adjusted to minimize the objective function given by

$$\chi^2 = \frac{(T_{1,c} - T_{1,e})^2}{\sigma_{T_1}^2} + \frac{(T_{2,c} - T_{2,e})^2}{\sigma_{T_2}^2} + \frac{(NOE_c - NOE_e)^2}{\sigma_{NOE}^2} \tag{6}$$

where subscripts c and e denote calculated and experimental values, respectively, and σ is the error of the individual relaxation parameters.

To improve the reliability of the fits for backbone amide NMR relaxation data of CTnC·2Ca^{2+}·Rp40, the 500 and 600 MHz data sets were combined into a single set and fit using Bayesian statistical methods developed by Andrec et al. (*59*). One advantage of Bayesian statistical methods is that no particular model selection is made relative to the data. Furthermore, the analysis is not subject to convergence problems, which may arise when fitting using classical approaches. The data were fit to the $S^2-\tau_e-R_{ex}$ model (with a τ_m of 7.36 ns), which represents the most parametrized form of the single-time scale model. Given that R_{ex} is expected to increase with the square of the magnetic field for genuine chemical exchange, R_{ex} was restrained such that $R_{ex}^{600} = (6/5)^2 R_{ex}^{500}$.

The marginal density of S^2 for the *i*th residue, $P(S^2|R_i)$, was calculated with the program Mathematica using the function Nintegrate. The limits of the integral for the calculation of $P(S^2|R_i)$ were set from 0 to 100 ms for τ_e and from 0 to 5 s for R_{ex}. The prior probability, $P(S^2, \tau_e, R_{ex}, \tau_m)$, was taken to be equal to 1 in the region defined by $0 \leq S^2 \leq 1$, $\tau_e \geq 0$, $R_{ex} \geq 0$, and 0 outside this region. For each residue, the value of S^2 was incremented in steps of 0.05, and the marginal density of S^2, $P(S^2|R_i)$, was calculated for a minimum of 21 S^2 values, 10 points around a central point, whose value had a priori been estimated from a classical fit using the $S^2-\tau_e$ model. For each residue, S^2 and its associated uncertainty were calculated by plotting $P(S^2|R_i)$ as a function of S^2 and fitting the curve to a Gaussian distribution.

Structure-Based Thermodynamic Calculations for Rp40 Binding to CTnC·2Ca^{2+}. The STC program (*60*) was used to calculate the thermodynamics of binding of Rp40 to CTnC·2Ca^{2+}. The crystal structures of TnC·2Ca^{2+}·TnI$_{1-47}$ (*34*) and TnC·4Ca^{2+} (*11*), both determined using rabbit skeletal TnC, not chicken skeletal TnC as in the current study, were used as reference structures for the protein−ligand and free protein structures, respectively. The coordinates of the C-domain in both structures were isolated by removal of the coordinates corresponding to residues 1−85

of the N-domain. Residues 86−91 of CTnC form an α-helix in the original structure of TnC·4Ca^{2+} (*11*), but were given an extended conformation using the InsightII program (*61*) to better reflect the lack of secondary structure in this region when CTnC is isolated from the N-domain.

The crystal structure of TnC·2Ca^{2+}·TnI$_{1-47}$ only includes residues 3−33 of TnI (*34*); thus, structure-based thermodynamic calculations may not properly reflect the correct binding situation with Rp40 using the X-ray coordinates. Residues 1, 2, and 34−47 of TnI$_{1-47}$ are believed to be disordered in the crystal. Also, there are no structural data for unbound Rp40. Thus, it was assumed that residues 1, 2, and 34−40 are unstructured in the free state, and therefore do not contribute to entropy changes upon binding, and we have used the structure of TnI$_{3-33}$ from the crystal structure as a model for the free peptide structure to perform the structure-based thermodynamic calculations for estimating the affinity of binding of Rp40 to CTnC·2Ca^{2+}. This assumption might not be valid since secondary structure prediction using the program Peptool (*62*) indicates that Rp40 is 95% helical, spanning residues 2−39. Additionally, binding of Rp40 to CTnC·2Ca^{2+} may lead to structuring of the C-terminal end of the peptide, assuming that the C-terminal end of the peptide is unstructured in the free state, and this would contribute significantly to the thermodynamics of binding.

Details for the structure-based thermodynamic calculations are similar to those reported by Lavigne et al. (*60*). The standard entropy of dissociation ΔS_d^0 for protein dissociation can be expressed as the sum of the changes in the following: solvation entropy (ΔS_{sol}), conformational entropy (ΔS_{conf}), and overall rotational/translational entropy (ΔS_{rt}):

$$\Delta S_d^{\ 0} = \Delta S_{sol}(T) + \Delta S_{conf} + \Delta S_{rt} \tag{7}$$

The entropic contribution of solvation (ΔS_{sol}) is temperature-dependent and can be calculated from changes in accessible surface area of nonpolar (ΔASA_{np}) and polar residues (ΔASA_{pol}) (*60, 63*). The change in conformational entropy (ΔS_{conf}) can be decomposed according to

$$\Delta S_{conf} = \Delta S_{bu \to ex} + \Delta S_{ex \to u} + \Delta S_{bb} \tag{8}$$

where $\Delta S_{bu \to ex}$ is the gain in conformational entropy for a side chain upon exposure, following disordering of tertiary or quaternary interactions, $\Delta S_{ex \to u}$ is the change in conformational entropy of the side chain corresponding to secondary structure unfolding, and ΔS_{bb} corresponds to the gain in conformational entropy for unfolding of the backbone. For structure-based thermodynamic calculations, we enhanced the STC program to allow the inclusion of the contribution from backbone conformational entropy (ΔS_{bb}) as calculated from backbone amide ^{15}N NMR relaxation data for the CTnC·2Ca^{2+}·Rp40 complex. Due to a lack of experimental backbone amide ^{15}N relaxation data for the peptide, ΔS_{bb} for Rp40 was not included. The STC program was further adapted to incorporate the conformational entropy contribution of the side chains ($\Delta S_{ex \to u}$) based on the change in accessible surface area of side chains (ASA$_{sc}$) when the secondary structure unfolds according to

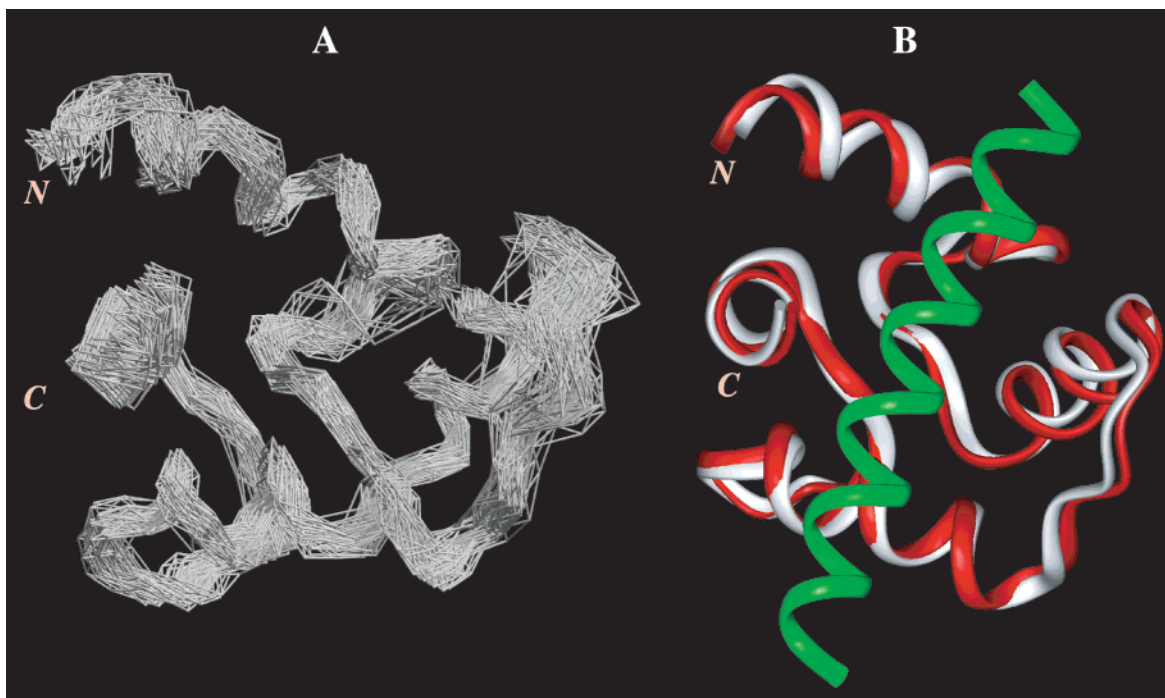$$\Delta S_{ex \to u} = (\Delta ASA_{sc}/\Delta ASA_{sc*})\Delta S_{ex \to u*} \tag{9}$$

FIGURE 1: (A) Ensemble of 30 solution structures of CTnC·2Ca^{2+} in the CTnC·2Ca^{2+}·Rp40 complex superimposed onto the average structure of CTnC·2Ca^{2+} (only residues 94−158 are shown). (B) Ribbon representation of the minimized average solution structure of CTnC·2Ca^{2+}·Rp40 (red) superimposed on the crystal structure of TnC·2Ca^{2+}·TnI$_{1-147}$ (white). TnI$_{1-147}$ is shown in green (only residues 6−29 are shown). It was not possible to determine the structure of Rp40 within the CTnC·2Ca^{2+}·Rp40 complex.

where ΔASA_{sc*} and $\Delta S_{ex \rightarrow u*}$ are standard values reported by Miller et al. (*64*) and D'Aquino et al. (*63*).

RESULTS

Structure of CTnC·2Ca^{2+}·Rp40 Determined by NMR Spectroscopy. The 30 lowest-energy structures of CTnC·2Ca^{2+} in the CTnC·2Ca^{2+}·Rp40 complex were generated with 873 NOE-derived distances restraints, 86 dihedral angle restraints, and 11 distance restraints to the Ca^{2+} ions, and are shown superimposed in Figure 1A. The average structure is compared to the C-domain of TnC in the X-ray structure of TnC·2Ca^{2+}·TnI$_{1-47}$ (*34*) in Figure 1B. The structural statistics for the ensemble of solution structures are given in Table 2. The distribution of NOEs (intraresidue, sequential, medium-range, and long-range) and the backbone atom rmsd values relative to the average structure for each residue are provided in Figure 2. Backbone rmsd values were calculated from the 30 lowest-energy structures after superimposition of the backbone atoms of residues 95−158 of CTnC in the CTnC·2Ca^{2+}·Rp40 complex onto the average structure. The mean backbone rmsd from the average structure for residues 95−157 of CTnC·2Ca^{2+} in the CTnC·2Ca^{2+}·Rp40 complex is 0.77 ± 0.17 using all residues in that region, 0.63 ± 0.14 with residues having a backbone rmsd of <1.0, and 0.80 ± 0.17 with residues having a backbone rmsd of >1.0. The quality of the ensemble of solution structures was analyzed with the program Procheck (*54*). Eighty-five percent of the residues in well-defined regions were found to be in most favored ϕ and ψ regions of the Ramachandran map, with another 15% in additional allowed regions. There were no NOE violations greater than 0.2 Å. A total of seven different distance violations in the range of 0.1−0.2 Å were detected in seven different structures of the family of 30 structures, and therefore, no structure had more than one distance
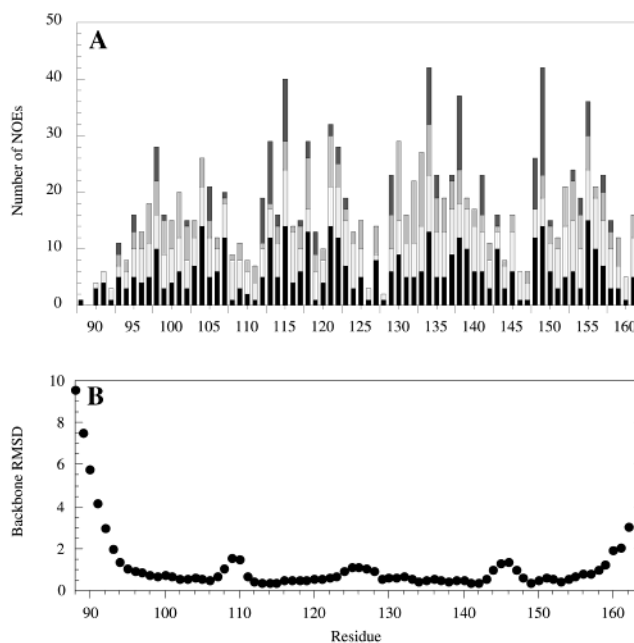

FIGURE 2: (A) Distribution of NOEs as a function of residue number. Intraresidue, sequential, medium-range, and long-range NOEs are identified by black, white, slight gray, and dark gray columns, respectively. (B) Backbone rmsd for the ensemble of 30 solution structures with respect to the average coordinates.

violation. Only one dihedral violation of >1° in one structure was detected within the final ensemble of structures. The structure of CTnC·2Ca^{2+} in complex with Rp40 is very similar to the C-domain of TnC·2Ca^{2+} in complex with TnI$_{1-47}$ (*34*), as previously determined by X-ray crystallography (backbone rmsd of 1.0 upon superimposition of residues 95−158). A comparison of the angles between α-helices within CTnC in the CTnC·2Ca^{2+}·Rp40 complex and the CTnC·2Ca^{2+}·TnI$_{1-47}$ complex in Table 3 indicates

Table 3: Interhelical Angles for CTnC·2Ca^{2+} (skeletal and cardiac isoforms) Free and Bound to N-Terminal TnI Peptides

helix pair	bound			free		
	CTnC·2Ca^{2+}·Rp40[a]	cCTnC·2Ca^{2+}·TnI$_{33-80}$[e]	TnC·2Ca^{2+}·TnI$_{1-47}$[b]	TnC·4Ca^{2+} [d]	cCTnC·2Ca^{2+} [f]	TnC·2Ca^{2+} [c]
E/F	93 ± 7	82 ± 4	100	89 ± 6	114 ± 4	108
E/G	132 ± 7	157 ± 7	134	137 ± 6	122 ± 5	124
E/H	112 ± 6	112 ± 3	116	110 ± 5	114 ± 5	122
F/G	127 ± 5	120 ± 5	122	133 ± 6	117 ± 3	126
F/H	41 ± 6	59 ± 4	47	36 ± 6	42 ± 4	33
G/H	115 ± 3	87 ± 5	107	107 ± 7	122 ± 4	111

[a] Using residues 95−105, 115−124, 131−141, and 151−158 for helices E−H, respectively (PDB entry 1JC2). [b] Using residues 91−103, 112−120, 128−138, and 148−155 for helices E−H, respectively (PDB entry 1A2X) (*34*). [c] Using residues 89−105, 115−125, 131−142, and 151−159 for helices E−H, respectively (PDB entry 5TNC) (*7*). [d] Using residues 96−105, 115−124, 131−141, and 151−157 for helices E−H, respectively (PDB entry 1TNW) (*9*). [e] Using residues 95−103, 114−123, 130−138, and 150−156 for helices E−H, respectively (PDB entry 1GGS) (*30, 31*). [f] Using residues 95−102, 114−123, 132−139, and 151−157 for helices E−H, respectively (PDB entry 3CTN) (*90*).
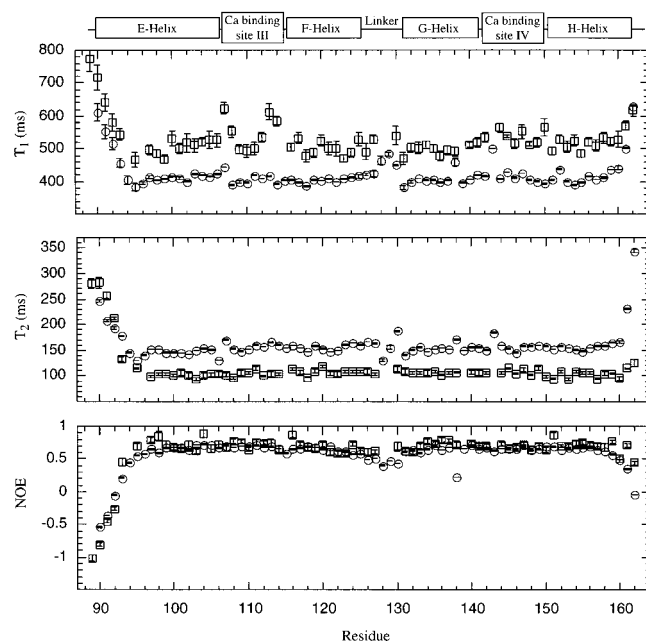

FIGURE 3: Backbone amide ^{15}N NMR relaxation times for CTnC·2Ca^{2+} (○) at 1.33 mM and CTnC·2Ca^{2+}·Rp40 (□) at 0.33 mM and at a magnetic field strength corresponding to a ^{1}H Larmor frequency of 500 MHz.

that no significant change occurs in the degree of structural "openness", or exposure of the hydrophobic patch of CTnC·2Ca^{2+} upon binding of Rp40.

Backbone Amide ^{15}N Relaxation Data. Backbone amide ^{15}N NMR relaxation data for CTnC·2Ca^{2+} at 500 MHz were analyzed for 73 of 75 residues. The backbone resonances of M^{88} and M^{89} were not observed due to rapid exchange with water. Partial resonance overlap for residues S^{94} and I^{115}, E^{96} and K^{139}, and V^{129} and K^{143} in the ^{1}H−^{15}N HSQC NMR spectra restricted the relaxation data analysis for the [^{15}N]-CTnC·2Ca^{2+}·Rp40 complex to 67 residues at 500 and 600 MHz. The ^{15}N−^{1}H$_N$ backbone amide resonance of H^{128} could not be assigned in the ^{1}H−^{15}N HSQC NMR spectra.

The experimental backbone amide ^{15}N relaxation values for [^{15}N]CTnC·2Ca^{2+} and [^{15}N]CTnC·Ca^{2+}·Rp40 are shown in Figure 3. The T_1, T_2, and NOE values of [^{15}N]CTnC·2Ca^{2+} show similar patterns in comparison to those of the cardiac isoform [^{15}N]cNTnC·Ca^{2+}, where large deviations from average values are observed at both the N- and C-termini (the first and last residues of helices E and H, respectively), as well as in the FG linker and calcium binding sites III and IV, to a smaller extent. These regions correspond structurally

to helices A and D (helices E and H in the C-domain), the BC linker (FG linker in the C-domain), and Ca^{2+} binding sites I and II (analogous to sites III and IV in the C-domain), which were shown to be the most flexible parts of [^{15}N]-cNTnC·Ca^{2+} (*38*). The average measured backbone relaxation parameters are listed in Table 4. Residues whose internal motions affect their measured T_1 values were excluded from the calculation of the averages, as determined using NOE criteria. For example, residues with NOE values smaller than 0.6 at 500 MHz and smaller than 0.65 at 600 MHz were rejected. For CTnC·2Ca^{2+} in the absence of Rp40, this included residues 89−96, 98, 115, 124−130, 133, 138, and 159−162, which are located at the N- and C-termini, the FG linker, and the Ca^{2+} binding sites. For CTnC·2Ca^{2+}·Rp40, residues 89−93, 122, 123, 160, and 162 were excluded.

Figure 3 indicates that binding of Rp40 perturbs the dynamics of CTnC by reducing backbone flexibility in the Ca^{2+} binding sites and, more strikingly, at the C-terminal end of helix H, as judged by changes in the overall pattern of the T_1, T_2, and NOE values plotted as a function of residue number. For [^{15}N]cNTnC·Ca^{2+}·Rp40 at 0.33 mM, a second data set was collected at 600 MHz to evaluate the quality of the data. Figure 4 illustrates different relaxation parameter ratios per residue for backbone amide ^{15}N relaxation data collected at 500 and 600 MHz. The statistics for residues whose relaxation is not significantly affected by internal motions (NOE^{500} > 0.6 and NOE^{600} > 0.65) are listed in Table 4. As expected, the average T_1^{600}/T_1^{500} ratio (1.24 ± 0.05) is >1, but the pattern of the T_1 data is constant throughout the sequence. Figure 4B indicates that T_2^{500} and T_2^{600} are equivalent for the majority of residues. The average T_2^{600}/T_2^{500} (0.98 ± 0.05) is slightly less than 1, consistent with theoretical predictions that indicate that the contribution from dipole−dipole relaxation ($T_{2,DD}$) should be almost identical at both fields, whereas chemical shift anisotropy will contribute more to T_2 relaxation ($T_{2,CSA}$) with increasing magnetic field strengths. The T_1/T_2 ratios from which τ_m was calculated are plotted in Figure 4C. The average NOE^{600}/NOE^{500} ratio (1.06 ± 0.1) is larger than 1, which is also consistent with theoretical predictions. Taking into account the fact that the average S^2 for structured regions in proteins is usually around 0.85 at ∼30 °C, and assuming isotropic overall rotational tumbling for a 7.32 kDa protein and a τ_e ranging from 0 to 100 ps, the $S^2-\tau_m-\tau_e$ model predicts that NOE^{600}/NOE^{500} ranges from 0.98 to 1.03, which is in agreement with the average experimental value.

Table 4: Experimental Backbone Amide ^{15}N Relaxation Parameters and Overall Rotational Correlation Times (τ_m) at 500 and 600 MHz for [^{15}N]CTnC in the Ca^{2+}-Saturated State and Bound to Rp40[a]

	[^{15}N]CTnC·2Ca^{2+} (1.33 mM)	[^{15}N]CTnC·2Ca^{2+}·Rp40		
		1.33 mM	0.65 mM	0.33 mM
T_1^{500} (ms)	410 ± 18 (0.4%)	571 ± 31 (0.9%)	−	518 ± 32 (3.2%)
T_2^{500} (ms)	154 ± 8 (0.5%)	96 ± 4 (1%)	−	105 ± 5 (2.7%)
NOE^{500}	0.67 ± 0.03 (0.7%)	0.71 ± 0.03 (3%)	−	0.71 ± 0.06 (8.4%)
T_1^{600} (ms)	−	694 ± 42 (0.81%)	649 ± 40 (1.7%)	639 ± 38 (1.9%)
T_2^{600} (ms)	−	90 ± 5 (0.88%)	101 ± 5 (1.1%)	103 ± 5 (1.9%)
NOE^{600}	−	0.75 ± 0.03 (2%)	0.76 ± 0.04 (4%)	0.75 ± 0.05 (6.0%)
T_1^{600}/T_1^{500}	−	1.22 ± 0.03	−	1.24 ± 0.05
T_2^{600}/T_2^{500}	−	0.94 ± 0.03	−	0.98 ± 0.05
T_1^{500}/T_2^{500}	−	6.0 ± 0.5	−	4.9 ± 0.4
T_1^{600}/T_2^{600}	−	7.7 ± 0.7	−	6.3 ± 0.6
NOE^{600}/NOE^{500}	−	1.06 ± 0.05	−	1.06 ± 0.1
τ_m^{500} (ns)	4.78 ± 0.11	8.52 ± 0.24	−	7.56 ± 0.22
τ_m^{600} (ns)	−	8.25 ± 0.26	7.42 ± 0.30	7.32 ± 0.15

[a] The numbers in parentheses correspond to the average errors on individual T_1, T_2, and NOE values from which the average was calculated.
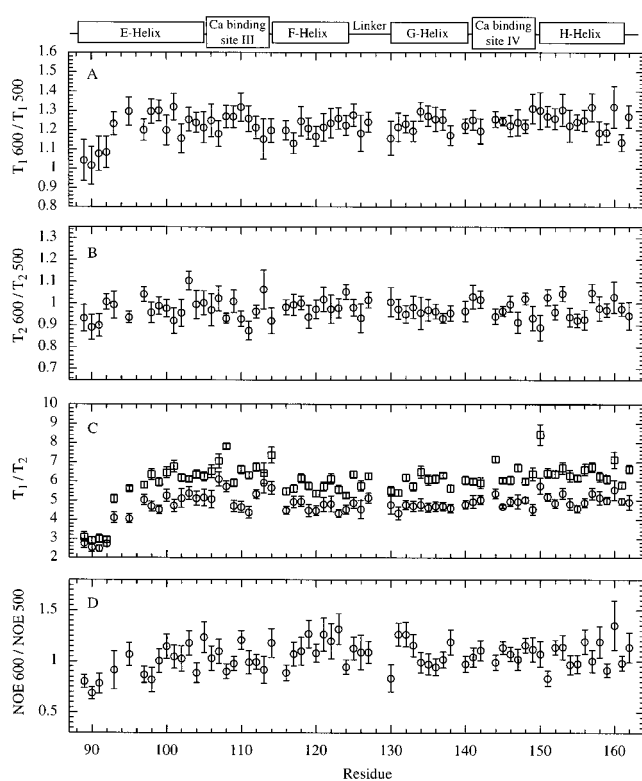
FIGURE 4: Backbone amide ^{15}N NMR relaxation time ratios for CTnC·2Ca^{2+}·Rp40 (○) at 0.33 mM and at magnetic field strengths corresponding to ^{1}H Larmor frequencies of 500 and 600 MHz. In panel C, the T_1/T_2 ratios are identified by squares at 600 MHz and by circles at 500 MHz.

Determination of the Overall Rotational Correlation Time. Backbone amide ^{15}N NMR relaxation data were interpreted using the Lipari−Szabo model-free approach (*41, 42*). From the normalized values of the principal axes of the inertia tensor, 1.6/1.07/1.0 for CTnC·2Ca^{2+} (*7*) (calculated from the crystal structure of TnC·4Ca^{2+}) and 1.32/1.07/1.0 for CTnC·2Ca^{2+}·Rp40 (*34*) (using coordinates from the crystal structure of TnC·2Ca^{2+}·TnI$_{1−47}$), the overall rotational tumbling was initially assumed to be isotropic. The overall macromolecular correlation time (τ_m) was determined using two different methods. In the first approach, τ_m was determined using an in-house Mathematica script (P. Mercier) from the T_1/T_2 ratio of residues falling within one standard deviation of the mean, after removal of residues whose NOE value was lower than

a given threshold (NOE^{500} > 0.6, NOE^{600} > 0.65). This ensures the elimination of residues whose relaxation is affected by fast internal motions on the picosecond time scale. The overall correlation time was determined by optimizing a χ^2 function given by

$$\chi^2 = \sum_{i=1}^{N}\left(\frac{(T_{1i}/T_{2i})_e - (T_{1i}/T_{2i})_c}{\sigma_{T_{1i}/T_{2i}}}\right) \tag{10}$$

over the N remaining residues. The subscripts e and c denote experimental values and predicted values, respectively.

In the second approach, individual residues were fit to the $S^2 - \tau_m - \tau_e$ model, including fitting the experimental NOE values, and where τ_m was adjusted separately for each residue. A global τ_m was obtained from the average τ_m determined for each residue. Both methods gave identical results, which are summarized in Table 4.

The global correlation τ_m obtained for CTnC·2Ca^{2+} in the absence of Rp40 ($\tau_m = 4.8 \pm 0.1$ ns) is in good agreement with the expected value ($\tau_m \sim 4.5$ ns) for isotropic tumbling on the basis of the molecular mass [τ_m(ns) $\sim$ MW(kDa)/2]. However, since the calculated τ_m (8.52 ± 0.24 ns at 500 MHz and 8.25 ± 0.26 ns at 600 MHz) for CTnC·2Ca^{2+}·Rp40 at 1.33 mM was larger than the expected value (6.8 ns) assuming isotropic tumbling, and on the basis of the molecular mass, the sample was diluted 2-fold twice, and a full set of ^{15}NT_1, ^{15}NT_2, and {^{1}H}−^{15}N NOE data were acquired for each dilution. Figure 5 shows the value of τ_m as a function of concentration for the CTnC·2Ca^{2+}·Rp40 complex. τ_m was fit to a monomer−dimer equilibrium, giving a dimerization constant (K_{dimer}) of ~8.3 mM. Thus, the percent dimer is estimated to be 20% at 1.33 mM, 12% at 0.65 mM, and 7% at 0.33 mM. The monomer−dimer equilibrium occurs in the fast exchange limit on the NMR time scale; thus, at 0.33 mM, the peak intensities in the ^{15}NT_1, ^{15}NT_2, and ^{1}H−^{15}N HSQC NMR spectra are heavily weighted toward the monomeric species, and were fit to a single-exponential, two-parameter decay. The global τ_m extracted from the experimental backbone amide ^{15}N relaxation data thus reflects the weighted average corresponding to the proportions of monomer and dimer, and is weighted mostly toward the monomeric τ_m.

Using criteria established by Tjandra et al. (*65*), the rotational diffusion anisotropy of CTnC·2Ca^{2+}·Rp40 was
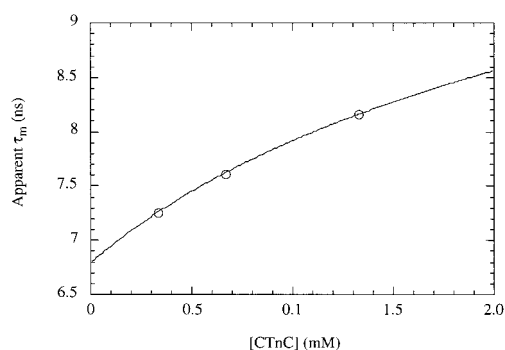
FIGURE 5: Global rotational correlation time (τ_m) for CTnC·2Ca^{2+}·Rp40 as a function of concentration. The curve was fit to a monomer−dimer equilibrium, yielding a dimerization constant of 8.3 mM.

Table 5: Rotational Diffusion Anisotropy for CTnC·2Ca^{2+}·Rp40

	500 MHz[a]	500 MHz[b]	600 MHz[a]	600 MHz[b]
$D_\parallel/D_\perp$	1.10 ± 0.03	1.14	1.10 ± 0.01	1.16
E^c	20 ± 1	94.3	94 ± 2	12.8
$E_v{}^c$	0.94 ± 0.06	3.8	3.49 ± 0.08	0.68
$F_x{}^c$	2.7 ± 0.6	3.1	2.5 ± 0.3	6.8

[a] Using atom coordinates from the ensemble of NMR structures. [b] Using atom coordinates from the X-ray structure of TnC·2Ca^{2+}·TnI$_{1-47}$ (*34*). [c] E, E_v, and F_x are as defined in Table 2 of ref *39*.

examined using residues not affected by fast picosecond and slower millisecond time scale motions. An average T_1/T_2 ratio was first calculated with residues having NOEs of >0.6 at 500 MHz and NOEs of >0.65 at 600 MHz. Residues having a T_1/T_2 ratio outside the range defined by the mean ± one standard deviation, or located in random-coil secondary structure elements and the β-sheets region, were excluded. The analysis was carried out using a program written in house (*39*) with 25 and 31 residues at 500 and 600 MHz, respectively. The degree of anisotropy was calculated with respect to isotropic, axially symmetric, and fully asymmetric rotational tumbling models using atomic coordinates derived from the 30 solution structures of CTnC·2Ca^{2+}·Rp40 determined herein and the crystal structure of TnC·2Ca^{2+}·TnI$_{1-47}$ (*34*). The statistics of the analysis are reported in Table 5. On the basis of the observation that the degree of anisotropy was found to be small ($D_\parallel/D_\perp \sim 1.1$) and that the improvement in χ^2 was not meaningful according to a statistical *F* test, the model-free analysis was carried out assuming isotropic rotational tumbling.

Determination of Backbone Amide ^{15}N S^2 *Values.* For [^{15}N]CTnC·2Ca^{2+} in the absence of Rp40, the experimental relaxation parameters (^{15}NT_1, ^{15}NT_2, and {^{1}H}−^{15}N NOE) for each residue were fit to five motional models, using the Lipari−Szabo model-free analysis as implemented in the program Tensor 2 (see Experimental Procedures) (*66*). The changes in S^2 between CTnC·2Ca^{2+} and CTnC·2Ca^{2+}·Rp40 are discussed in detail below.

Due to the presence of dimer, the backbone amide ^{15}N NMR relaxation data for the CTnC·2Ca^{2+}·Rp40 complex at 0.33 mM were fit using different methods. The 500 and 600 MHz data sets were first fit separately using the program Tensor 2 (*66*), using the model-free approach as described above. To verify the validity of the results, the two data sets were then combined and fit simultaneously using the $S^2−\tau_m−\tau_e−R_{ex}$ model using Bayesian analysis (*59*). The details

of the procedure utilized herein differ slightly from the original paper (see Experimental Procedures). For residues having a $P(S^2|R_i)$ close to 0 or significantly lower than the values observed for other residues, the experimental data were evaluated using a two-time scale model. The use of a two-time scale model greatly increased the $P(S^2|R_i)$ values for residues 89−91, 93, 95, 97, 103, 116, 117, 119−121, 123, 124, 126, 131, 133, 138, and 161. The S^2 values determined by independent analysis of the two data sets at 500 and 600 MHz using the standard model-free approach within the Tensor 2 program, and the S^2 values determined using Bayesian analysis for the combined data, are in agreement with each other. The results of Bayesian statistical analysis for extraction of S^2, τ_e, and R_{ex} values for F^{112} are presented in Figure 6.

Protein dimerization is known to result in values of S^2 that are larger than the true values. Schurr et al. have shown, using simulated data, that the best-fit S^2 values are closer to their actual values when τ_m is allowed to float for each residue, rather than using a global correlation time for the entire protein (*67*). The fits were shown to be excellent for pure monomers or dimers, but the best-fit internal motion parameters were judged as being unreliable when the fraction of monomer was between 0.9 and 0.2. Given that the proportion of monomer is >0.9 for 0.33 mM CTnC·2Ca^{2+}·Rp40, and the degree of rotational tumbling anisotropy is small compared to that in cases investigated by Schurr et al., the 500 and 600 MHz relaxation data sets, as well as the data set that is a combination of the two, were fit to the $S^2−\tau_e−\tau_m$ model using the protocol recommended by Schurr et al. (*67*), where τ_m is independently evaluated for each residue. The S^2 values were consistent with the ones determined by the standard protocol where a global τ_m value is used, except for residues needing the two-time scale model or R_{ex} terms to properly fit the relaxation data. For this reason, S^2 values obtained using a global τ_m are reliable. The S^2 values determined from the Bayesian analysis using the data set formed by the union of the 500 and 600 MHz data sets were chosen as final values for CTnC·2Ca^{2+}·Rp40. The combined data set is potentially more reliable because the fitted parameters are overdetermined. The backbone amide S^2 values obtained for CTnC·2Ca^{2+} in the absence and in the presence of Rp40 are presented in panels A and B of Figure 7, and the change in S^2 for CTnC·2Ca^{2+} on a per residue basis upon Rp40 binding is shown in Figure 7C. The crystallographic *B* factors of the backbone nitrogen atoms of TnC in the TnC·2Ca^{2+}·TnI$_{1-47}$ (*34*) complex are also shown in Figure 7B, for qualitative comparison to S^2 values. Intuitively, one might expect a correlation between backbone S^2 values and *B* factors, as conformational disorder in the crystal structure may be indicative of enhanced mobility in solution. However, the two parameters are not directly or linearly correlated (*68*).

Backbone Conformational Entropy Changes upon Peptide Binding Determined from Changes in S^2. The free energy change (ΔG) associated with the binding of a ligand to a protein dictates the binding affinity. Changes in both enthalpy (ΔH), or structure, and entropy (ΔS), or dynamics, contribute to the energetics of the interaction.

Building on the work of Akke et al. (*69*), Yang and Kay (*70*) developed a methodology for correlating changes in conformational entropy associated with bond vector fluctua-
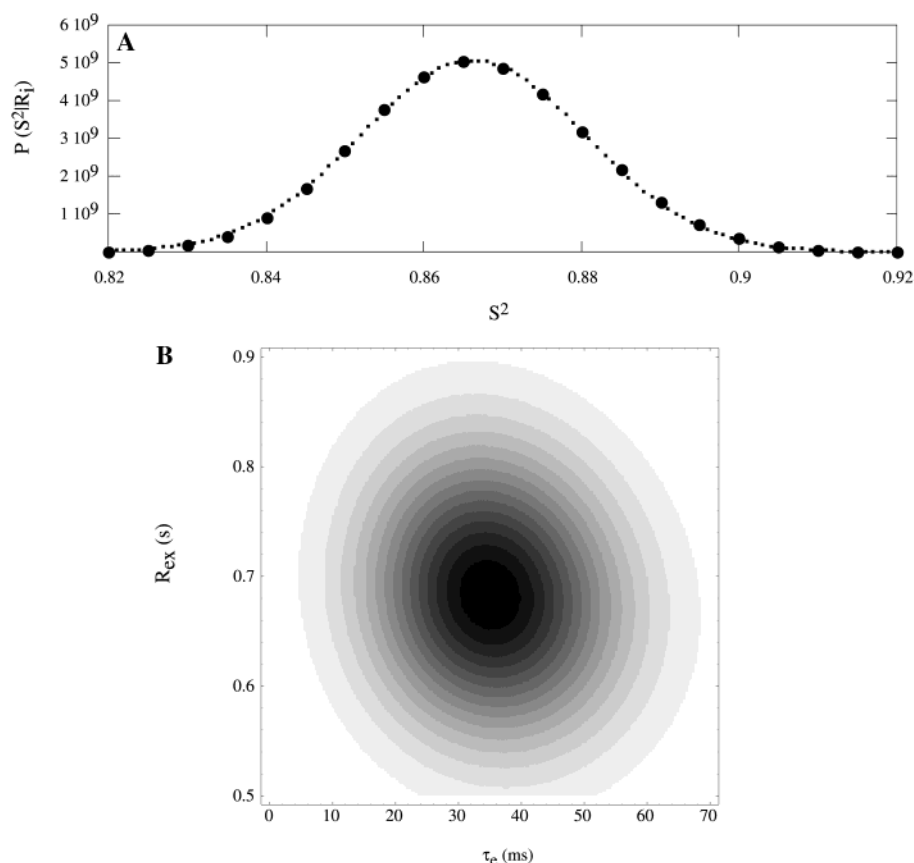
FIGURE 6: (A) Marginal density, $P(S^2|R_i)$, as a function of S^2 for residue F^{112} [(●) calculated values and (·) predicted values with a Gaussian distribution centered at $S^2 = 0.866$ with $\sigma = 0.014$)]. (B) Surface density plot of the marginal density of S^2 integrated over R_{ex} and τ_e for residue F^{112} (the plot was generated with S^2 set to 0.866). The darker region represents τ_e and R_{ex} values that reproduce the experimental relaxation parameters with the highest probability.

tions on the nanosecond to picosecond time scale with a two-state transition. From S^2 values determined from backbone amide ^{15}N NMR relaxation data of CTnC·2Ca^{2+}, the contribution of conformational entropy can be calculated according to

$$\frac{\Delta S_p(j)}{k} = \ln\left(\frac{3 - \sqrt{1 + 8S_b}}{3 - \sqrt{1 + 8S_a}}\right) \quad (11)$$

where k is Boltzmann's constant, $\Delta S_p(j)$ is the entropy change associated with the jth backbone $^{15}N-^1H_N$ vector, and S_a and S_b are the square root of the Lipari–Szabo order parameter for states a (CTnC·2Ca^{2+}) and b (CTnC·2Ca^{2+}·Rp40), respectively. The contribution to free energy from changes in backbone conformational entropy, on a per residue basis, was calculated from the changes in backbone amide ^{15}N S^2 values and is shown in Figure 7D. A value of 9.6 ± 0.7 kcal mol^{-1} ($-T\Delta S$) at 30 °C is obtained by summing the individual contribution for each residue. At present, it is not clear if the motion for each residue is independent, and given that NMR-derived S^2 values are not sensitive to motions outside the picosecond to millisecond time scale, or translational motion, and that separability of these motions is assumed, the analysis of thermodynamics from NMR relaxation data can only be performed in a semiquantitative manner. For this reason, the value of 9.6 ± 0.7 kcal mol^{-1} ($-T\Delta S$) for the change in backbone conformational entropy reported here is an approximation, and should be viewed as

an upper limit. Nevertheless, according to this result, the binding of Rp40 is entropically unfavorable, as the backbone of CTnC·2Ca^{2+} "stiffens" upon Rp40 binding. The observation that the backbone flexibility of CTnC·2Ca^{2+} is reduced upon binding of Rp40 is in agreement with the common notion that binding should reduce flexibility, perhaps for the backbone of a protein, but particularly for the side chains (71). Interestingly, cases have been reported in the literature where backbone amide ^{15}N S^2 values decrease upon ligand binding (72), which is counterintuitive (73), but may very well be a critically important factor in contributing favorably to ligand binding.

Structure-Based Thermodynamic Calculations for Rp40 Binding to CTnC·2Ca^{2+}. The entropic contribution to the thermodynamics of Rp40 binding to CTnC·2Ca^{2+} was estimated from structure-based thermodynamic calculations using the program STC (60) (see Experimental Procedures). The results obtained from the structure-based thermodynamic calculations using STC (Table 6) indicate that the binding of Rp40 to CTnC·2Ca^{2+} is entropically favorable. This result highlights the importance of other entropic factors apart from changes in conformational entropy that play a role in the determination of the binding affinity.

The total decrease in accessible surface area for nonpolar residues (ΔASA_{np}) upon complex formation is more than 200% greater than the decrease in the accessible surface area of polar residues (ΔASA_{pol}), and therefore, solvation entropy is the dominant term in eq 12. When Rp40 binds, the total
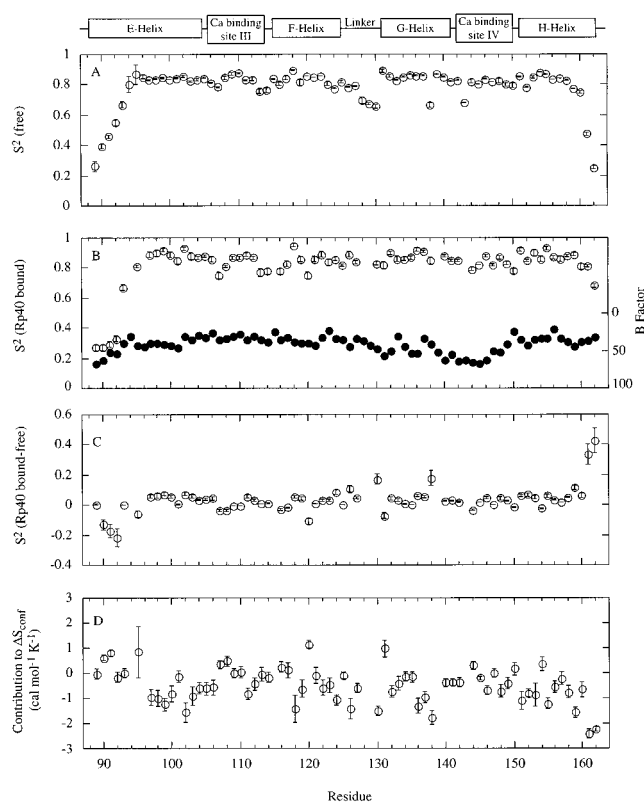
FIGURE 7: Backbone amide ^{15}N S^2 on a per residue basis for CTnC·$2Ca^{2+}$ (○) at 1.33 mM (A) and CTnC·$2Ca^{2+}$·Rp40 at 0.33 mM (B). Changes in S^2 values for CTnC·$2Ca^{2+}$ observed upon Rp40 binding (C). Contribution to conformational entropy on a per residue basis (D). The crystallographic B factors (●) for the nitrogen atoms of TnC in the TnC·$2Ca^{2+}$·TnI$_{1−47}$ (*34*) complex are included in panel B for qualitative comparison.

Table 6^a

(A) Change in Accessible Surface Area for Polar (ΔASA_{pol})
and Nonpolar Residues (ΔASA_{np}) upon Rp40 Binding to
CTnC·$2Ca^{2+}$ Used for Structure-Based Thermodynamic Calculations

species	ΔASA_{pol} (Å^2)	ΔASA_{np} (Å^2)
Rp40	222	740
CTnC·$2Ca^{2+}$	513	771
total	735	1511

(B) Structure-Based Thermodynamic Analysis
for Binding of Rp40 to CTnC·$2Ca^{2+}$

$\Delta C_{p\text{bind}}$ (cal mol^{-1} K^{-1})	489
ΔH_{bind} (kcal mol^{-1})	4.33
ΔS_{bind} (cal mol^{-1} K^{-1})	42
ΔS_{sol} (cal mol^{-1} K^{-1})	144
ΔS_{rt} (cal mol^{-1} K^{-1})	−8
ΔS_{conf} (cal mol^{-1} K^{-1})	−94
$\Delta S_{\text{bu}\rightarrow\text{ex}}$ (cal mol^{-1} K^{-1})	−47
$\Delta S_{\text{ex}\rightarrow\text{u}}$ (cal mol^{-1} K^{-1})	−15
ΔS_{bb} (cal mol^{-1} K^{-1})	−32
$-T\Delta S_{\text{bind}}$ (kcal mol^{-1})	−12.68
ΔG_{bind} (kcal mol^{-1})	−8.35
K_a (mM^{-1})	1.05
K_d (μM)	0.95

^{a} Positive values indicate a decrease in accessible surface area upon complex formation.

hydrophobic surface area of CTnC·$2Ca^{2+}$ decreases by 771 Å^2, from 3053 to 2282 Å^2. Since the structure of CTnC·$2Ca^{2+}$ in the CTnC·$2Ca^{2+}$·Rp40 complex is similar to the structure of unbound CTnC·$2Ca^{2+}$, most of the diminution in accessible nonpolar surface area can be attributed to a

reduction in the size of the hydrophobic patch of CTnC·$2Ca^{2+}$ that is formed by the core residues of CTnC·$2Ca^{2+}$. The hydrophobic patch of CTnC·$2Ca^{2+}$ forms the binding interface for Rp40. The positive gain in entropy achieved by burying hydrophobic residues upon complex formation ($\Delta S_{\text{sol}} = 144$ cal mol^{-1} K^{-1}) compensates, in large part, for the cost associated with a decrease in backbone flexibility ($\Delta S_{\text{bb}} = -31.9 \pm 2.3$ cal mol^{-1} K^{-1} for CTnC·$2Ca^{2+}$ upon Rp40 binding from backbone amide ^{15}N relaxation data) and the burial of side chains ($\Delta S_{\text{bu}\rightarrow\text{ex}} = -47$ cal mol^{-1} K^{-1}). The structure-based thermodynamic calculations were carried out with coordinates for TnI$_{1−33}$ in the free state taken from the crystal structure. This yields a dissociation constant of 0.95 μM. This value is close to the value determined by following chemical shift changes of the backbone amide ^{1}H−^{15}N resonances of CTnC·$2Ca^{2+}$ upon titration with Rp40 peptide (2 ± 1 μM) (*22*). If the last seven residues of Rp40 do not indeed contribute significantly to the binding of Rp40, the agreement between the two results suggests that the structure of Rp40 does not change considerably upon binding.

Interestingly, structure-based thermodynamic calculations performed without considering the contribution of backbone and side chain conformational entropy lead to a binding constant of 2×10^{-9} μM, which is unrealistically tight binding, thus emphasizing the importance of including the contribution of conformational entropy when performing structure-based thermodynamic calculations for high-affinity protein−ligand complexes. In light of the extent of the decrease in flexibility for the backbone of CTnC·$2Ca^{2+}$ upon binding to Rp40, and its importance in the calculation of thermodynamic parameters, it is likely that conformational entropy changes for the peptide backbone upon complex formation with CTnC·$2Ca^{2+}$ also play an important role. A decrease in TnI$_{3−33}$ backbone flexibility upon binding to CTnC·$2Ca^{2+}$ would contribute to an increase in the value of the dissociation constant (0.95 μM).

DISCUSSION

The general role of TnC in regulating muscle contraction is now quite well understood (*1−6*). However, no high-resolution structures of TnC with TnI and/or TnT are available, and the specific interactions occurring between members of the troponin complex during different stages of muscle contraction still need to be elucidated. In the past few years, we have successfully determined the solution structures of TnC in various states, and in complex with different peptides of TnI, for both the skeletal and cardiac isoforms (*9, 10, 25, 28, 48, 49*). These studies, coupled with backbone and side chain NMR relaxation data (*38, 39*), have provided insight into the mechanism and energetics of Ca^{2+} and peptide binding to TnC. The collective efforts of different research groups have allowed for the construction of different models for the interactions between different components of the TnI·TnC·TnT ternary complex (*21, 74, 75*).

The Ca^{2+}-binding sites of the C-domain of TnC are believed to always be occupied by either Mg^{2+} or Ca^{2+} under physiological conditions. Due to the high affinity of Ca^{2+} for the ion binding sites of the C-domain of TnC, this domain is believed to assume a structural role within intact muscle. On the other hand, the N-terminal domain of TnC does not bind metal ions in the resting state of intact muscle. In

addition, association of Ca^{2+} with the N-terminal Ca^{2+}-specific regulatory sites of TnC is thought to give rise to conformational changes within TnC that essentially constitutes the molecular switch that initiates muscle contraction. Classification of the roles for the C- and N-terminal domains as structural and regulatory, respectively, may not reflect the genuine physiological roles of the two domains of TnC within intact muscle. Functional studies by the Hodges group have indicated that CTnC may participate to some extent in the regulation of muscle contraction by interacting with different regions of TnI in the resting and contracted states (*21*). Following Ca^{2+} binding to NTnC, the inhibitory TnI peptide, TnI_{96-115}, is believed to switch binding partners, from actin to TnC, thus removing the steric block on actin, and allowing for myosin binding and completion of the power stroke.

A key component of the inhibitory mechanism of contraction is arguably the binding location and structure of TnI_{96-115}. A study involving ^{1}H chemical shift perturbations by NMR led to the proposal that $TnI_{104-115}$ forms a short helix, distorted around two central proline residues, and interacts with the hydrophobic patch on $CTnC \cdot 2Ca^{2+}$ (*76*). The $CTnC \cdot 2Ca^{2+} \cdot TnI_{104-115}$ complex was subsequently modeled with the short TnI peptide anchored in the hydrophobic pocket of TnC (*18*). A more recent study using both NMR and CD spectroscopic data by Trewella et al. indicates that $TnI_{104-115}$ adopts an extended conformation when bound to TnC (*33*).

Recently, it has been demonstrated that while $TnI_{116-131}$ is bound to NTnC, TnI_{95-115} can displace the Rp40 peptide from TnI when it is bound to $CTnC \cdot 2Ca^{2+}$ in intact TnC (*21*). This result somewhat contradicts a previous study by the same research group, which shows that Rp40 can prevent intact TnI binding to intact TnC (*36*). It was proposed that $TnI_{116-131}$ modulates TnI_{96-115} binding to TnC and that it might contribute to displacement of Rp40 from TnC. On the basis of this hypothesis, the authors proposed that the hydrophobic patch of CTnC alternately binds TnI_{96-115} in the presence of Ca^{2+}-saturated NTnC, and the N-terminal region of TnI (Rp40) under conditions of low Ca^{2+} concentrations. However, more recent studies question this model for the TnI−TnC interaction, as described in detail in the following discussion. First, in a previous paper (*22*), we showed that in the absence of NTnC and $TnI_{116-131}$, the binding affinity of Rp40 for TnC was ∼24 times larger than that of TnI_{96-115} ($K_{d-Rp40} = 2 \pm 1$ μM, $K_{d-TnI_{96-115}} = 47 \pm 7$ μM). By following chemical shift changes with [1]H−^{15}N HSQC NMR spectroscopy, we have also suggested that the peptides share common binding sites on TnC. However, the changes in backbone amide [1]H−[15]N chemical shifts induced by TnI_{96-115} binding did not indicate that the peptide is bound within the hydrophobic patch of TnC (*18*) but, rather, binds across the top of one end of the hydrophobic patch. On the other hand, the location of Rp40 deduced from backbone amide [1]H−[15]N chemical shift mapping matches perfectly the binding site of TnI_{1-47} as determined by X-ray diffraction (*34*). Our results also clearly demonstrate that Rp40 prevents TnI_{96-115} from binding to $CTnC \cdot 2Ca^{2+}$ and completely displaces TnI_{96-115} from $CTnC \cdot 2Ca^{2+}$.

Fluorescence resonance energy transfer and chemical photo-cross-linking studies with the TnI·TnC intact binary complex and the intact ternary complex (TnI·TnC·TnT) have led to important conclusions that support a structural role for the N-terminal region of TnI rather than a functional role (*75, 77*). The distance between residue 6 of TnI and residue 89 of TnC was shown to be Ca^{2+}-independent, which is not consistent with a regulatory mechanism involving movement of Rp40 in and out of the hydrophobic patch of $CTnC \cdot 2Ca^{2+}$.

In this paper, we present the solution structure of $CTnC \cdot 2Ca^{2+}$ bound to Rp40 and examine changes induced in backbone dynamics of $CTnC \cdot 2Ca^{2+}$ upon Rp40 binding. The superimposition of the 30 lowest total energy structures determined by NMR, presented in Figure 1A, shows that the structure is well-defined from residue 94 to 160, with somewhat increased rmsds from the average backbone atom positions for the two Ca^{2+}-binding loops. As shown in Figure 2A, the smaller number of distance restraints per residue for regions close to the Ca^{2+}-binding loops is likely to be responsible for increased rmsd values in these regions, rather than increased backbone flexibility in comparison to the rest of the protein (see Figure 7B). The linker region is relatively well-defined compared to regions of secondary structure for $CTnC \cdot 2Ca^{2+}$ bound to Rp40. As shown in Figure 1B, the average structure calculated from a family of 30 structures (Figure 1A) is similar to that for the crystal structure of $TnC \cdot 2Ca^{2+} \cdot TnI_{1-47}$. As reported in Table 3, both the structure of $CTnC \cdot 2Ca^{2+} \cdot Rp40$ determined herein and the structure of $TnC \cdot 2Ca^{2+} \cdot TnI_{1-47}$ determined by X-ray crystallography show a similar degree of openness, interpreted in terms of interhelical angles between helices within CTnC. Helices E and F are slightly more closed in comparison to those in the solution structure of $TnC \cdot 4Ca^{2+}$ determined by NMR (*9*), but show similar interhelical angles with respect to the structure of $TnC \cdot 2Ca^{2+}$ determined by X-ray crystallography (*7*). Whereas a slight opening of CTnC was observed in the cardiac isoform of the $CTnC \cdot 2Ca^{2+} \cdot TnI_{33-80}$ complex with respect to $CTnC \cdot 2Ca^{2+}$ (*30, 31*), there is no significant change in the degree of structural openness for the skeletal isoform of $CTnC \cdot 2Ca^{2+}$ upon Rp40 binding reported herein.

The structure and sites of interaction of Rp40 bound to $CTnC \cdot 2Ca^{2+}$ could not be determined in this study. Attempts to obtain ^{1}H chemical shift assignments for the bound peptide through the use of 2D [13]C- and ^{15}N-filtered experiments were unrewarding, primarily due to the fact that the peptide resonances were overlapping. However, the unassigned [1]H$_\alpha$ chemical shifts (*78, 79*) are indicative of an α-helical structure for Rp40 in the complex, in agreement with X-ray structural studies (*34*). Moreover, the residues for which NOE peaks observed in the simultaneous 3D ^{13}C/^{15}N NOESY-HSQC experiment that did not have the expected symmetrical cross-peak and therefore expected to be NOEs between protein and peptide also correspond to residues that are in proximity to the peptide in the crystal structure of $TnC \cdot 2Ca^{2+} \cdot TnI_{1-47}$ (*34*). Figure 8 shows strip plots for residue I^{104} from TnC taken from the simultaneous 3D ^{13}C/^{15}N NOESY-HSQC experiment. I^{104} is within 2 Å of 47 different peptide protons in the X-ray structure, and is therefore a key residue in terms of the number of contacts with the target protein TnC [the analogous residue from rabbit TnC is I^{101} which is used for the crystal structure determination (*34*)]. For CTnC, I^{104} is also the residue for which the largest number of [1]H−[1]H contacts to Rp40 could
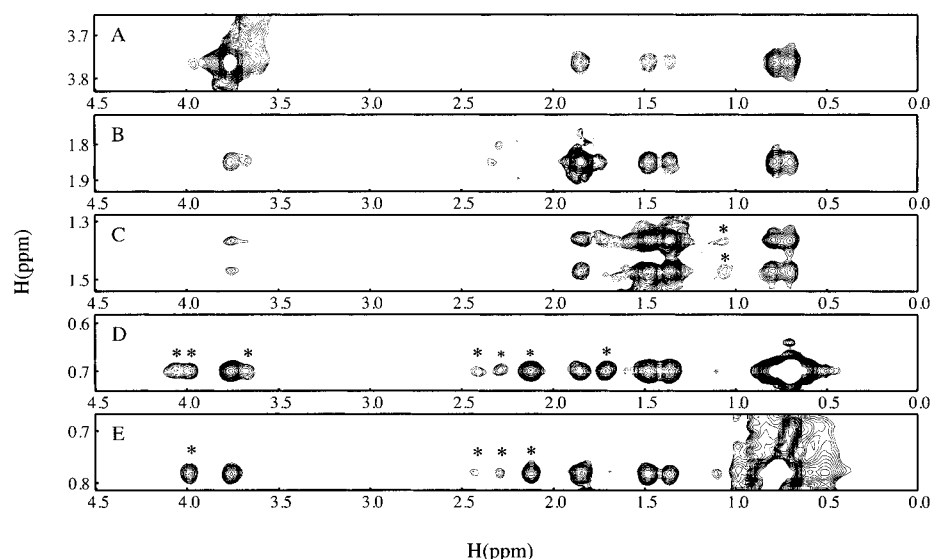
FIGURE 8: Strip plots taken at side chain ^{13}C chemical shifts for residue I^{104} [(A) ^{13}C$_\alpha$, (B) ^{13}C$_\beta$, (C) ^{13}C$_\gamma$, and (D and E) ^{13}C$_{\delta1,\delta2}$] from the ^{13}C part of the simultaneous 3D ^{13}C/^{15}N NOESY-HSQC spectrum. Asterisks denote cross-peaks lacking symmetry-related cross-peaks, and therefore are likely to be NOE contacts between CTnC·2Ca^{2+} and Rp40.

be observed by NMR in this study, followed by residues T^{125} and V^{161} from TnC. Residue T^{125}, corresponding to S^{122} in rabbit TnC, is not a key residue involved in the binding of TnI$_{1−47}$ to TnC, as judged by number of proton contacts observed between this residue and TnC in the crystal structure. The side chain of V^{161} of TnC participates in several hydrophobic contacts, and this has implications for changes in the flexibility for the C-terminal helix H.

Backbone amide ^{15}N relaxation measurements indicate concentration-dependent dimerization for the CTnC·2Ca^{2+}· Rp40 complex in solution. Unlike NTnC·2Ca^{2+} that tends to self-associate at millimolar concentrations (*80*), CTnC· 2Ca^{2+} is not known to self-associate in solution. Interestingly, the structure of calmodulin in complex with the peptide GAD$_p$ [CAM·(GAD$_p$)$_2$] has been recently reported (*81*). The complex was shown to dimerize via GAD$_p$ and possessed a 2-fold symmetry axis, with two GAD$_p$ peptide units forming a cross. Like the peptide-induced dimerization observed for calmodulin, we propose that Rp40 may be responsible for the observed dimerization of the CTnC·2Ca^{2+}·Rp40 complex, possibly via helix−helix interactions of Rp40 with itself. While the structural determination of CTnC·2Ca^{2+} in the CTnC·2Ca^{2+}·Rp40 complex was performed at a concentration that would include 20% dimer, the ^{1}H−^{1}H NOE data do not indicate the presence of a dimeric form.

The binding of Rp40 to CTnC·2Ca^{2+} results in a decrease in flexibility for CTnC, particularly at the C-terminal end of helix H, where the largest changes in S^2 (see Figure 7C) and backbone amide ^{1}H−^{15}N chemical shifts (*22*) are observed. The tight binding of Rp40 to CTnC·2Ca^{2+} contributes to a reduction in the amount of conformational space that is sampled by the extreme C-terminal end of CTnC·2Ca^{2+}. The flexibility of the linker between helices F and G is also reduced, and this was also observed in a study with the corresponding cardiac complex [cCTnC· 2Ca^{2+}·TnI$_{33−80}$ (*30, 31*)]. However, with the cardiac isoform, the flexibility at the C-terminal end of cCTnC was not affected by the binding of N-terminal TnI peptides (TnI$_{33−80}$ and TnI$_{1−80}$) in the absence (*30, 31*) and presence of the

cardiac-specific TnI 33-residue N-terminal extension (*82*). This might be the result of a difference in the affinities of binding to their corresponding CTnC isoforms between the cardiac TnI peptide and the skeletal TnI peptide, and could also indicate slight differences in CTnC residues between the two isoforms that make contact with their respective TnI peptides.

The contribution of pico- to nanosecond time scale backbone amide ^{15}N−^{1}H bond vector motions to conformational entropy, as derived from NMR relaxation data, indicates that binding of Rp40 to CTnC·2Ca^{2+} is an entropically unfavorable event. However, approximation of other entropic factors (such as solvation entropy) with structure-based thermodynamic calculations using the program STC indicates that the overall change in entropy upon binding is positive and overcomes the enthalpy term, which is positive and unfavorable. Thus, structure-based thermodynamic calculations indicate that the binding reaction is driven by a large positive increase in solvation entropy, as hydrophobic side chains are buried upon complex formation. The large decrease in accessible hydrophobic surface area for nonpolar residues appears to be a critical factor determining the thermodynamics governing binding of Rp40 to CTnC·2Ca^{2+}, at least when estimating thermodynamic parameters from structure. The large increase in solvent entropy is responsible, in part, for overcoming the entropic penalty associated with a reduction in the flexibility for the backbone of CTnC·2Ca^{2+} (measured here using backbone amide ^{15}N NMR relaxation measurements), and potential decreases in flexibility for the protein and peptide side chains upon formation of the CTnC·2Ca^{2+}·Rp40 complex.

NOTE ADDED AFTER ASAP POSTING

This article was inadvertently released ASAP on 8/01/01 before final corrections were made. Changes to the HNHB nuclei in Table 1 and the units for K_a in Table 6B were made. The correct version was posted 8/21/01.

REFERENCES

1. Squire, J. M., and Morris, E. P. (1998) *FASEB J. 12*, 761–771.
2. Filatov, V. L., Katrukha, A. G., Bulargina, T. V., and Gusev, N. B. (1999) *Biochemistry (Moscow) 64*, 969–985.
3. Finn, B. E., and Drakenberg, T. (1999) *Adv. Inorg. Chem. 46*, 441–494.
4. Gergely, J. (1998) *Adv. Exp. Med. Biol. 453*, 169–176.
5. Perry, S. V. (1999) *Mol. Cell. Biochem. 190*, 9–32.
6. Gordon, A. M., Homsher, E., and Regnier, M. (2000) *Physiol. Rev. 80*, 853–924.
7. Herzberg, O., and James, M. N. G. (1988) *J. Mol. Biol. 203*, 761–779.
8. Satyshur, K. A., Rao, S. T., Pyzalska, D., Drendal, W., Greaser, M., and Sundaralingam, M. (1988) *J. Biol. Chem. 263*, 1628–1647.
9. Slupsky, C. M., and Sykes, B. D. (1995) *Biochemistry 34*, 15953–15964.
10. Gagné, S. M., Tsuda, S., Li, M. X., Smillie, L. B., and Sykes, B. D. (1995) *Nat. Struct. Biol. 2*, 784–789.
11. Houdusse, A., Love, M. L., Dominguez, R., Grabarek, Z., and Cohen, C. (1997) *Structure 5*, 1695–1711.
12. Kretsinger, R. H. (1976) *Annu. Rev. Biochem. 45*, 239–266.
13. Szczesna, D., Guzman, G., Miller, T., Zhao, J., Farokhi, K., Ellemberger, H., and Potter, J. D. (1996) *J. Biol. Chem. 271*, 8381–8386.
14. Gagné, S. M., Li, M. X., McKay, R. T., and Sykes, B. D. (1998) *Biochem. Cell Biol. 76*, 301–312.
15. Olah, G. A., Rokop, S. E., Wang, C.-L. A., Blechner, S. L., and Trewhella, J. (1994) *Biochemistry 33*, 8233–8239.
16. Olah, G. A., and Trewhella, J. (1994) *Biochemistry 33*, 12800–12806.
17. Stone, D. B., Timmins, P. A., Schneider, D. K., Krylova, I., Ramos, C. H. I., Reinach, F. C., and Mendelson, R. A. (1998) *J. Mol. Biol. 281*, 689–704.
18. Ngai, S.-M., Sönnichsen, F. D., and Hodges, R. S. (1994) *J. Biol. Chem. 269*, 2165–2172.
19. Pearlstone, J. R., and Smillie, L. B. (1995) *Biochemistry 34*, 6932–6940.
20. Pearlstone, J. R., and Smillie, L. B. (1997) *Biophys. J. 72*, A331.
21. Tripet, B. P., Van Eyk, J. E., and Hodges, R. S. (1997) *J. Mol. Biol. 271*, 728–750.
22. Mercier, P., Li, M. X., and Sykes, B. D. (2000) *Biochemistry 39*, 2902–2911.
23. McKay, R. T., Tripet, B. P., Pearlstone, J. R., Smillie, L. B., and Sykes, B. D. (1999) *Biochemistry 38*, 5478–5489.
24. McKay, R. T., Tripet, B. P., Hodges, R. S., and Sykes, B. D. (1997) *J. Biol. Chem. 272*, 28494–28500.
25. McKay, R. T., Pearlstone, J. R., Corson, D. C., Gagné, S. M., Smillie, L. B., and Sykes, B. D. (1998) *Biochemistry 37*, 12419–12430.
26. McKay, R. T. (1999) in *Department of Biochemistry*, University of Alberta, Edmonton, AB.
27. Li, M. X., Spyracopoulos, L., and Sykes, B. D. (1998) *Biophys. J. 74*, A51.
28. Li, M. X., Spyracopoulos, L., and Sykes, B. D. (1999) *Biochemistry 38*, 8289–8298.
29. Finley, N., Abbott, M. B., Abusamhadneh, E., Gaponenko, V., Dong, W., Gasmi-Seabrook, G., Howarth, J. W., Rance, M., Solaro, R. J., Cheung, H. C., and Rosevear, P. R. (1999) *FEBS Lett. 453*, 107–112.
30. Gasmi-Seabrook, G. M., Howarth, J. W., Finley, N., Abusamhadneh, E., Gaponenko, V., Brito, R. M., Solaro, R. J., and Rosevear, P. R. (1999) *Biochemistry 38*, 14432.
31. Gasmi-Seabrook, G., Howarth, J. W., Finley, N., Abusamhadneh, E., Gaponenko, V., Brito, R. M., Solaro, R. J., and Rosevear, P. R. (1999) *Biochemistry 38*, 8313–8322.
32. Abbott, M. B., Dvoretsky, A., Gaponenko, V., and Rosevear, P. R. (2000) *FEBS Lett. 469*, 168–172.
33. Hernández, G., Blumenthal, D. K., Kennedy, M. A., Unkefer, C. J., and Trewhella, J. (1999) *Biochemistry 38*, 6911–6917.
34. Vassylyev, D. G., Takeda, S., Wakatsuki, S., Maeda, K., and Maeda, Y. (1998) *Proc. Natl. Acad. Sci. U.S.A. 95*, 4847–4852.
35. Syska, H., Wilkinson, J. M., Grand, R. J. A., and Perry, S. V. (1976) *Biochem. J. 153*, 375–387.
36. Ngai, S.-M., and Hodges, R. S. (1992) *J. Biol. Chem. 267*, 15715–15720.
37. Farrow, N. A., Muhandiram, R., Singer, A. U., Pascal, S. M., Kay, C. M., Gish, G., Shoelson, S. E., Pawson, T., Forman-Kay, J. D., and Kay, L. E. (1994) *Biochemistry 33*, 5984–6003.
38. Spyracopoulos, L., Gagné, S. M., Li, M. X., and Sykes, B. D. (1998) *Biochemistry 37*, 18032–18044.
39. Gagné, S. M., Tsuda, S., Spyracopoulos, L., Kay, L. E., and Sykes, B. D. (1998) *J. Mol. Biol. 278*, 667–686.
40. Spyracopoulos, L., Gagné, S. M., Gronwald, W., Kay, L. E., and Sykes, B. D. (1998) in *Proceedings for The International School of Structural Biology and Magnetic Resonance, 3rd Course on Protein Dynamics, Function and Design* (Jardetzky, O., and LeFeure, F. J., Eds.) pp 147–162, Plenum Press, New York.
41. Lipari, G., and Szabo, A. (1982) *J. Am. Chem. Soc. 104*, 4546–4559.
42. Lipari, G., and Szabo, A. (1982) *J. Am. Chem. Soc. 104*, 4559–4570.
43. Yang, D., Mok, Y. K., Forman-Kay, J. D., Farrow, N. A., and Kay, L. E. (1997) *J. Mol. Biol. 272*, 790–804.
44. Gagné, S. M., Tsuda, S., Li, M. X., Chandra, M., Smillie, L. B., and Sykes, B. D. (1994) *Protein Sci. 3*, 1961–1974.
45. Li, M. X., Gagné, S. M., Tsuda, S., Kay, C. M., Smillie, L. B., and Sykes, B. D. (1995) *Biochemistry 34*, 8330–8340.
46. Delaglio, F., Grzesiek, S., Vuister, G. W., Zhu, G., Pfeifer, J., and Bax, A. (1995) *J. Biomol. NMR 6*, 277–293.
47. Johnson, B. A., and Blevins, R. A. (1994) *J. Biomol. NMR 4*, 603–614.
48. Gagné, S. M., Li, M. X., and Sykes, B. D. (1997) *Biochemistry 36*, 4386–4392.
49. Spyracopoulos, L., Li, M. X., Sia, S. K., Gagné, S. M., Chandra, M., Solaro, R. J., and Sykes, B. D. (1997) *Biochemistry 36*, 12138–12146.
50. Kuboniwa, H., Grzesiek, S., Delaglio, F., and Bax, A. (1994) *J. Biomol. NMR 4*, 871–878.
51. Clore, G. M., Bax, A., and Gronenborn, A. M. (1991) *J. Biomol. NMR 1*, 13–22.
52. Kuszewski, J., Qin, J., Gronenborn, A. M., and Clore, G. M. (1995) *J. Magn. Reson., Ser. B 106*, 92–96.
53. Brünger, A. T. (1992) *X-PLOR, Version 3.1 A system for X-ray Crystallography and NMR*, Yale University Press, New Haven, CT.
54. Laskowski, R. A., MacArthur, M. W., Moss, D. S., and Thorton, J. M. (1993) *J. Appl. Crystallogr. 26*, 283–290.
55. Garrett, D. S., Powers, R., Gronenborn, A. M., and Clore, G. M. (1991) *J. Magn. Reson. 95*, 214–220.
56. Abragam, A. (1961) *Principles of Nuclear Magnetism*, Vol. 32, Oxford University Press, Toronto.
57. Clore, G. M., Szabo, A., Bax, A., Kay, L. E., Driscoll, P. C., and Gronenborn, A. M. (1990) *J. Am. Chem. Soc. 112*, 4989–4991.

58. Clore, G. M., Driscoll, P. C., Wingfield, P. T., and Gronenborn, A. M. (1990) *Biochemistry 29*, 7387−7401.
59. Andrec, M., Montelione, G. T., and Levy, R. M. (1999) *J. Magn. Reson. 139*, 408−421.
60. Lavigne, P., Bagu, J. R., Boyko, R., Willard, L., Holmes, C. F., and Sykes, B. D. (2000) *Protein Sci. 9*, 252−264.
61. *InsightII* (1995) Molecular Simulations Inc., San Diego.
62. Wishart, D. S., Stothard, P., and Van Domselaar, G. H. (2000) *Methods Mol. Biol. 132*, 93−113.
63. D'Aquino, J. A., Gomez, J., Hilser, V. J., Lee, K. H., Amzel, L. M., and Freire, E. (1996) *Proteins 25*, 143−156.
64. Miller, S., Janin, J., Lesk, A. M., and Chothia, C. (1987) *J. Mol. Biol. 196*, 641−656.
65. Tjandra, N., Wingfield, P., Stahl, S., and Bax, A. (1995) *J. Am. Chem. Soc. 117*, 12562−12566.
66. Dosset, P., Hus, J. C., Blackledge, M., and Marion, D. (2000) *J. Biomol. NMR 16*, 23−28.
67. Schurr, J. M., Babcock, H. P., and Fujimoto, B. S. (1994) *J. Magn. Reson., Ser. B 105*, 211−224.
68. Powers, R., Clore, G. M., Garrett, D. S., and Gronenborn, A. M. (1993) *J. Magn. Reson., Ser. B 101*, 325−327.
69. Akke, M., Bruschweiler, R., and Palmer, A. G. (1993) *J. Am. Chem. Soc. 115*, 9832−9833.
70. Yang, D., and Kay, L. E. (1996) *J. Mol. Biol. 263*, 369−382.
71. Lee, A. L., Kinnear, S. A., and Wand, A. J. (2000) *Nat. Struct. Biol. 7*, 72−77.
72. Zidek, L., Novotny, M. V., and Stone, M. J. (1999) *Nat. Struct. Biol. 6*, 1118−1121.
73. Forman-Kay, J. D. (1999) *Nat. Struct. Biol. 6*, 1086−1087.
74. Tung, C. S., Wall, M. E., Gallagher, S. C., and Trewhella, J. (2000) *Protein Sci. 9*, 1312−1326.
75. Luo, Y., Wu, J. L., Li, B., Langsetmo, K., Gergely, J., and Tao, T. (2000) *J. Mol. Biol. 296*, 899−910.
76. Campbell, A. P., and Sykes, B. D. (1991) *J. Mol. Biol. 222*, 405−421.
77. Luo, Y., Leszyk, J., Li, B., Gergely, J., and Tao, T. (2000) *Biochemistry 39*, 15306−15315.
78. Wishart, D. S., and Sykes, B. D. (1994) *Methods Enzymol. 239*, 363−392.
79. Wishart, D. S., Sykes, B. D., and Richards, F. M. (1991) *J. Mol. Biol. 222*, 311−333.
80. Spyracopoulos, L., Gagné, S. M., and Sykes, B. D. (2001) in *Proceedings for the International School of Structural Biology and Magnetic Resonance, 4th Course on Protein Dynamics, Function and Design* (Jardetzky, O., and Lefevre, J. F., Eds.) pp 37−44, Plenum Press, New York.
81. Yap, K. L., Yuan, T., Vogel, H. J., and Ikura, M. (2001) in *Keystone Symposia-Frontiers of NMR in Molecular Biology VII*.
82. Gaponenko, V., Abusamhadneh, E., Abbott, M. B., Finley, N., Gasmi-Seabrook, G., Solaro, R. J., Rance, M., and Rosevear, P. R. (1999) *J. Biol. Chem. 274*, 16681−16684.
83. Muhandiram, D. R., and Kay, L. E. (1994) *J. Magn. Reson., Ser. B 103*, 203−216.
84. Kay, L. E., Keifer, P., and Saarinen, T. (1992) *J. Am. Chem. Soc. 114*, 10663−10665.
85. Zhang, O., Kay, L. E., Olivier, J. P., and Forman-Kay, J. D. (1994) *J. Biomol. NMR 4*, 845−858.
86. Kay, L. E., Xu, G. Y., Singer, A. U., Muhandiram, D. R., and Forman-Kay, J. D. (1993) *J. Magn. Reson., Ser. B 101*, 333−337.
87. Pascal, S. M., Muhandiram, D. R., Yamazaki, T., Forman-Kay, J. D., and Kay, L. E. (1994) *J. Magn. Reson.*, Ser. B *103*, 197−201.
88. Archer, S. J., Ikura, N. I., Torchia, D. A., and Bax, A. (1991) *J. Magn. Reson. 95*, 636−641.
89. Ogura, K., Terasawa, H., and Inagaki, F. (1996) *J. Magn. Reson., Ser. B 112*, 63−68.
90. Sia, S. K., Li, M. X., Spyracopoulos, L., Gagné, S. M., Liu, W., Putkey, J. A., and Sykes, B. D. (1997) *J. Biol. Chem. 272*, 18216−18221.